Spontaenous Emission in Systems of Reduced Dimension

by

Tyler A. Hill

A dissertation submitted in partial fulfillment
of the requirements for the degree of
Doctor of Philosophy
(Physics)
in The University of Michigan
2018

Doctoral Committee:

Associate Professor Hui Deng, Chair
Professor Paul Berman
Associate Professor P.C. Ku
Professor Roberto Merlin
Professor John Schotland

Tyler A. Hill
hityler@umich.edu
ORCID iD: 0000-0002-8896-8686

ACKNOWLEDGEMENTS

Getting a doctorate is a long journey - and I would like to thank the many people that I have met along the way, without them this work would not be possible.

First I would like to thank my advisor - Professor Hui Deng. She displayed endless patience with my progress and lack thereof and my frequent confusion throughout the PhD. I am grateful for her wisdom and mentorship, and dedication to helping me become a better scientist. Under her guidance the research group felt like a family striving to reach common goals. Any time I had a question - she was always open and available for discussion. She also was instrumental in helping me form collaborations that proved vital to my progress and development towards my degree.

My fellow group members contributed greatly to my PhD.

I would like to thank Lei Zhang for helping to convince me to join him in Hui's group because the projects sounded so exciting. His enthusiasm and dedication to science helped inspire me to work hard, and I was a better graduate student when I tried to be more like him. He also taught me almost everything I know about actually carrying out experiments in an optics lab - I am very grateful for his kindness and knowledge. Lei is awesome.

I would like to thank Paul Bierdz for his friendship. Whenever I wanted to discuss an integral, a mathematical series, or had a random probability question that caught my eye - I could share my interest with Paul and he would care about what I cared about. My morale and sanity would not have been the same without him as a lab mate. Paul is fantastic.

I would like to thank Brandon Demory for keeping me sane during the many hours of late night experiments - and for letting me live after I told him the theory we had been working on together was full of holes right before his talk nearly every time we attended a conference together.

I would like to thank Bo Zhang for his great sense of humor - his positive energy and work ethic lifted the spirit of everyone around him.

I would like to thank Hoon - quiet yet quite funny, he and his wife Jia invited me to spend time with them and helped make the group feel like a family. Hoon is radical.

I would like to thank Joey. He was always thoughtful and hardworking - was easy to talk to and was someone you can count on.

I would like to thank Glenn - without his wacky sense and humor and dedication to his work the lab group would not be the same.

I would like to thank Eunice for listening to my lame stories, sometimes more than once, and laughing at my bad jokes. Having a friend in the lab helped keep me sane through some of the ups and downs of grad school.

I would like to thank (others) for (reasons).

I would like to thank the many students who I attempted to mentor - they all worked quite hard and constantly impressed me with their progress. Working with them was a highlight of my graduate career.

I would like to thank Professor Barry Sanders, who became almost like a second advisor and mentor to me during the second half of my studies. His words of encouragement gave me hope that somewhere in this world someone thought my work was interesting.

I would like to thank Youngmin for the time we had together - without which my life during grad school would not have been the same.

I would like to thank my friends Peter and Sung - who call me and make sure Im still alive.

Lastly I would like to thank my mom, dad, and siblings Autumn, Casey, A.J. and Summer - for being the best family anyone could ever ask for. Through the good times and the bad, they believed in me, stuck by me, supported me, and loved me. Thanks guys.

PREFACE

The work contained in this thesis was started around 2012 in collaboration with my friend and colleague Brandon Demory from P.C. Ku's group in the EECS department at the University of Michigan. Our goal was to make quantum dot emission brighter and faster with the aid of plasmonic coupling to silver, enhancing the emission of an entire 2-dimensional array of dots using a single silver coating [18].

Our work on this project attracted the attention of Professor Barry Sander's of the University of Calgary in 2014. He was interested in using our ability to make regular 2-dimensional arrays of quantum dots to study cooperate effects in 2 dimensions - i.e. superradiance phenomena, as he had recently worked with a group that had experimentally demonstrated cooperative effects in 1-dimension [84]. It turned out that our quantum dots were not a good candidate for experimental demonstration of cooperative effects in two dimensions due to issues with their inhomogeneity, so I began a theoretical investigation into how the phenomena would behave in two dimensions, which was unstudied unlike one dimensions [47] and three dimensions [49]. I discovered that the one, two, and thee dimensional theories could all be made to look alike, developing a theory of cooperative effects in any dimension [35].

TABLE OF CONTENTS

CHAPTER

LIST OF FIGURES

Figure

ABSTRACT

Matter coupled to light can emit photons. In the absence of an external field this process is known as spontaneous emission. The radiation properties depends in detail the nature of the emitter. In this thesis we consider a two level point-source emitter, and examine how the emission is affected by engineering the local environment.

We begin by studying analytically how embedding an emitter in a multi-layer cylindrical structure with radius much smaller than the emission wavelength alters the intensity of the emitted light. We find that for carefully chosen metal-dielectric interfaces, the emission can be strongly enhanced by the plasmonic effect.

With this intuition, we experimentally study an InGaN semiconductor quantum dot-in-wire structure as our two level emitter, and manipulate the local field environment by coupling to a lossy plasmonic cavity. We find that the strong enhancement of the field around the quantum dot due to the metal more than compensates for the non-radiative losses, leading to order-of-magnitude increases in the radiative spontaneous emission rate, as well as overall brightness.

We then examine how the emission of light can be affected by other nearby emitters. The cooperative effects are strongly dependent on the dimension of the system which controls the electromagnetic mode overlap of the emitters. We present a unified formalism capturing how these cooperative effects change from one dimension to the next.

Cooperative light scattering between emitters underpins collective effects such as super- and sub-radiance, and we numerically investigate how our previous results give rise to the key experimental signatures that can be used to identify those phenomena. Specifically, we study how the superadiant decay rate scales with the size of a 2-dimensional atomic cloud, and how cooperative effects between a small number of emitters alter the emission spectrum of strongly driven resonance fluorescence.

CHAPTER I

Introduction

In this work we study the effect of geometry on spontaneous emission processes. We pay particular attention to how the spontaneous emission of an emitter may be manipulated by changing the local environment with the addition of metal or dielectric materials, or by changing the effective dimension of the system using a structure to confine the electromagnetic field. We begin with a discussion of the physics underlying spontaneous emission, and then review means of obtaining approximate and exact analytic expressions for the spontaneous emission in terms of the classical electromagnetic field.

1.1 Spontaneous Emission

Spontaneous emission occurs when a quantum mechanical system emits photon when transitioning from a high energy state to a low energy state. It can occur in the absence of an external driving field. In this work we will be concerned with a 2-level quantum system. The rate of spontaneous emission is governed by Fermi's golden rule.

1.1.1 Fermi Golden Rule

Fermi's golden rule describes the transition probabilities of a system described by a Hamiltonian $H = H_0 + H'$, where H' is a perturbation of Hamiltonian H_0. Then if states $|i\rangle$ and $|j\rangle$ are energy eigenstates of H_0, the transition rate between these states is given by [24]

$$\Gamma_{i\to j} = \frac{2\pi}{\hbar}|\langle j|H|i\rangle|^2\rho(\nu) \tag{1.1}$$

where $\rho(\nu)$ is the density of photon states at frequency ν. Calculation of the transition rate then simply requires knowledge of the matrix element $|\langle j|H'|i\rangle|$ and ρ.

1.1.2 Purcell Effect

The Purcell effect describes how the spontaneous emission rate changes due to the presence of a cavity. In a cavity, the density of modes

$$\rho_c(\omega) = \frac{1}{\Delta\nu V} = \frac{1}{\nu}\frac{Q}{V}, \tag{1.2}$$

$$Q = \Delta\nu/\nu \tag{1.3}$$

where V is the volume of a single mode and $\Delta\nu$ is linewidth of the cavity (spacing between modes) and Q is the quality factor. The density of modes in 3-dimensional free space is [65]

$$\rho_f(\nu) = \frac{8\pi n^3\nu^2}{c^3}. \tag{1.4}$$

The Purcell factor F_p is the amount the emission rate increases in the cavity [65],

$$F_p = \frac{\Gamma_{i\to j,c}}{\Gamma_{i\to j,f}} = \frac{3}{4\pi^2}\left(\frac{\lambda}{n}\right)^3\frac{Q}{V} \propto \frac{\rho_c}{\rho_f}. \tag{1.5}$$

1.1.3 Radiative Enhancement

The Purcell factor measures the total change in the emission rate, but in general we have that [44]

$$\Gamma_{\text{tot}} = \Gamma_{\text{rad}} + \Gamma_{\text{nr}} + \Gamma_{\text{g}}, \tag{1.6}$$

where Γ_{rad} is the radiative decay, Γ_{nr} is the nonradiative decay, and Γ_{g} is the decay into guided modes of the system. We can isolate the radiative part following the treatment of [44] by examining the change in the electric field over time, which gives the emitted power

$$\begin{aligned} \left(\frac{\mathrm{d}E}{\mathrm{d}t}\right)_{\text{rad}} &= \frac{c}{8\pi} \int \left| \left(\boldsymbol{E}^{(0)} + \boldsymbol{E}^{(R)}\right) \times \left(\boldsymbol{H}^{(0)} + \boldsymbol{H}^{(R)}\right) \right|^2_{r\to\infty} r^2 \mathrm{d}\Omega, & (1.7) \\ &= \frac{ck^4}{3} |\boldsymbol{d}_{\text{tot}}|^2. & (1.8) \end{aligned}$$

Here $\boldsymbol{E}^{(0)}$ is the electric field in free space and $\boldsymbol{E}^{(R)}$ is the additional field from reflection off the cavity. From (1.8) we see that

$$\frac{\Gamma_{\text{rad}}}{\Gamma_0} = \frac{|\boldsymbol{d}_{\text{tot}}|^2}{|\boldsymbol{d}_0|^2}. \tag{1.9}$$

Here Γ_0 is the emission rate in free space and $\boldsymbol{d}_0$ is the free space dipole moment. Combining (1.8) and (1.9) we see that the radiative emission rate is proportional to the local field $\boldsymbol{E}$,

$$\Gamma_{\text{rad}} \propto |\boldsymbol{d}_0 \cdot \boldsymbol{E}|^2 \rho_f. \tag{1.10}$$

1.1.4 Quasistatic Approximation

In general to find the electric field in a given geometry it is necessary to solve for the dyadic Green's function from Maxwell's equations. However, significant implication can be made when all objects of interest have subwavelength spacing ($e^{ikr}/r \approx 1/r$), so that the field is essentially constant over this region. In that case, we can invoke the quasistatic approximation and find the electric field using scalar potentials, and have that the magnetic field $\boldsymbol{H} \approx 0$. In this case, there are only two Maxwell's equations

$$\nabla \cdot \boldsymbol{D} = \rho_C \tag{1.11}$$

$$\nabla \times \boldsymbol{E} = 0 \tag{1.12}$$

A dipole emitter has charge density [44, 11]

$$\rho_C = -\left(\boldsymbol{d}_0 \cdot \nabla'\right) \delta^{(3)}\left(\boldsymbol{r} - \boldsymbol{r}'\right) e^{-i\omega t} \tag{1.13}$$

In that case the electric field is given by

$$\boldsymbol{E} = -\nabla \left(\boldsymbol{d}_0 \cdot \nabla'\right) g(\boldsymbol{r}, \boldsymbol{r}'), \tag{1.14}$$

where the potential g is the solution to Poisson's equation with $\boldsymbol{r}$ being the position of the dipole in region with dielectric constant ϵ_1

$$\nabla^2 g = -\frac{1}{\epsilon_1} \delta^{(3)}(\boldsymbol{r} - \boldsymbol{r}'). \tag{1.15}$$

Here ∇' is the gradient with respect to the primed coordinates and we suppress the time dependence of the electric field. The radiative enhancement is then calculated

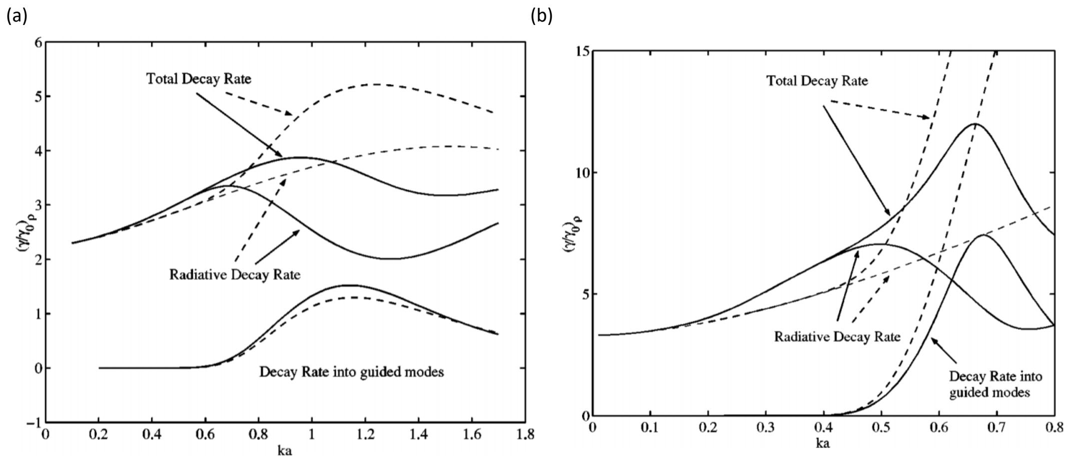

Figure 1.1: Images taken from [44]. This shows a comparison of the quasistatic approximation vs a full analytic solution in how in affects the spontaneous emission near a nanofiber. (a) The nanofiber has $\epsilon = 3$ (b) The nanofiber has $\epsilon = 10$.

using

$$\frac{\Gamma_{\text{rad}}}{\Gamma_0} = \left| \frac{\boldsymbol{d}_0 \cdot \boldsymbol{E}}{\boldsymbol{d}_0 \cdot \boldsymbol{E}_0} \right|^2 . \tag{1.16}$$

Numerical study on the quasistatic approximation's applicability shows it is very accurate for [44]

$$ka < 1/\epsilon. \tag{1.17}$$

As can be seen from Fig. 1.1 the quasi-static approximation remains reasonably accurate for $ka < 1/\sqrt{\epsilon}$.

1.2 Quantization of the electromagnetic field

Up to now we have discussed radiation from the perspective of quantum mechanics, but to understand cooperative light scattering phenomenon it will be necessary to delve into the realm of quantum electrodynamics, where light is described in terms of photons, which are modes of the electromagnetic field. To quantize the field, we begin with Maxwell's equations

$$\nabla \cdot \boldsymbol{B} = 0 \tag{1.18}$$

$$\nabla \cdot \boldsymbol{D} = \rho_f \tag{1.19}$$

$$\nabla \times \boldsymbol{E} = -\partial_t \boldsymbol{B} \tag{1.20}$$

$$\nabla \times \boldsymbol{H} = \boldsymbol{J}_f + \partial_t \boldsymbol{D} \tag{1.21}$$

and take the source terms $\boldsymbol{J}_f = 0$ and $\rho_f = 0$ Both the potential $\boldsymbol{A}$ and electric field $\boldsymbol{E}$ satisfy very similar wave equations

$$\left(\nabla^2 - \frac{1}{c^2}\partial_t^2\right)\boldsymbol{A} = 0 \tag{1.22}$$

$$\left(\nabla^2 - \frac{1}{c^2}\partial_t^2\right)\boldsymbol{E} = 0 \tag{1.23}$$

Because these fields satisfy a wave equation we can write them as a sum over modes of the field that satisfy the wave equation, and assume they satisfy a separable form

$$\boldsymbol{E}(\boldsymbol{r}, t) = \sum_{\boldsymbol{k},l} c_{\boldsymbol{k},l} u_{\boldsymbol{k},l}(\boldsymbol{r}) \hat{a}_{\boldsymbol{k},l}(t) + H.c. \tag{1.24}$$

The normalization constant can be found by requiring the electromagnetic field portion of the Hamiltonian appear as a harmonic oscillator

$$H_F = \frac{1}{8\pi}\int \left(|\boldsymbol{E}|^2 + |\boldsymbol{B}|^2\right) \mathrm{d}V := \sum_{\boldsymbol{k},l} \omega_{\boldsymbol{k},l}\left(\hat{a}^\dagger_{\boldsymbol{k},l}(t)\hat{a}_{\boldsymbol{k},l}(t) + \frac{1}{2}\right) \tag{1.25}$$

The 1/2 is the zero point energy and for the purposes of this thesis will be discarded. We then have

$$\boldsymbol{E}(\boldsymbol{r},t) = i \sum_{\boldsymbol{k},l} (2\pi\omega_{\boldsymbol{k},l})^{1/2} \left(\hat{a}_{\boldsymbol{k},l}(t) u_{\boldsymbol{k},l}(\boldsymbol{r}) + H.c.\right), \tag{1.26}$$

where the $u_{\boldsymbol{k},l}(\boldsymbol{r})$ have the normalization condition

$$\frac{1}{V}\int_V u^{\dagger}_{\boldsymbol{k},l}(\boldsymbol{r}) \cdot u_{\boldsymbol{k},l}(\boldsymbol{r}) \mathrm{d}V = 1 \tag{1.27}$$

Furthermore the operators $u_{\boldsymbol{k},l}(\boldsymbol{r})$ and $\hat{a}_{\boldsymbol{k},l}(t)$ satisfy the boundary conditions

$$\left(\nabla^2 + \frac{\omega^2_{\boldsymbol{k},l}}{c^2}\right) u_{\boldsymbol{k},l}(\boldsymbol{r}) = 0 \tag{1.28}$$

$$\left(\partial_t^2 + \omega^2_{\boldsymbol{k},l}\right) a_{\boldsymbol{k},l}(t) = 0 \tag{1.29}$$

The second equation implies harmonic $e^{i\omega_{\boldsymbol{k},l}t}$ time dependence of the photon creation operator $a_{\boldsymbol{k},l}$. The spatial mode $u_{\boldsymbol{k},l}(\boldsymbol{r})$ depends in detail upon the geometry of the system. One common choice is the quantize the field in a large box of volume V, with the requirement the field vanishes at the box boundary. In this case traveling waves satisfy (1.28) and we can write

$$\left\{\begin{matrix} \hat{\boldsymbol{E}}(\boldsymbol{r}) \\ \hat{\boldsymbol{B}}(\boldsymbol{r}) \end{matrix}\right\} = \sum_{\boldsymbol{k}} \sum_{l=1}^{2} \sqrt{\frac{2\pi\omega_{\boldsymbol{k},l}}{V}} \left\{\begin{matrix} \hat{\boldsymbol{e}}_l \\ \hat{\boldsymbol{k}} \times \hat{\boldsymbol{e}}_l \end{matrix}\right\} \left(\mathrm{e}^{\mathrm{i}\boldsymbol{k}\cdot\boldsymbol{r}} \hat{a}_{\boldsymbol{k}l}(t) + \mathrm{H.\,c.}\right) \tag{1.30}$$

Here the photon creation operator $\hat{a}^{\dagger}_{\boldsymbol{k}l}$ producing a photon with wavevector $\boldsymbol{k}$, frequency $\omega_{\boldsymbol{k},l}$, and polarization $\hat{\boldsymbol{e}}_l$, $\hat{\boldsymbol{k}} \cdot \hat{\boldsymbol{e}}_l = 0$.

1.3 Dyadic Green's function

As we saw in a previous section, the rate of spontaneous emission is proportional to the local electromagnetic field. In this previous section, we described an approximation for obtaining the electromagnetic field in the limit the object is very small. In general, we can obtain an exact result for the electromagnetic field using the method of Dyadic Green's functions.

We sketch the derivation of electromagnetic Green's functions Here. We begin by considering the relationships between the electromagnetic field and their vector potential $\boldsymbol{A}$ and scalar potential ϕ for a material with electric permittivity ϵ and magnetic permeability μ:

$$\begin{aligned} \boldsymbol{E}(\boldsymbol{r}) =& i\omega \boldsymbol{A}(r) - \nabla\phi(\boldsymbol{r}) \qquad (1.31) \\ \boldsymbol{H}(\boldsymbol{r}) =& \frac{1}{\mu}\nabla \times \boldsymbol{A}(\boldsymbol{r}) \qquad (1.32) \end{aligned}$$

Taking the curl of the microscopic Maxwell's equations we find the wave equation

$$\nabla \times \nabla \times \boldsymbol{A}(\boldsymbol{r}) = \mu \boldsymbol{J} - i\omega\mu\epsilon \left(i\omega \boldsymbol{A}(\boldsymbol{r}) - \nabla\phi(\boldsymbol{r})\right) \qquad (1.33)$$

We are still free to choose a gauge condition for $\boldsymbol{A}$, and for the simplicity of the Dyadic Green's function it will be convenient to choose Lorentz gauge

$$\nabla \cdot \boldsymbol{A}(\boldsymbol{r}) = i\omega\mu\epsilon\phi(\boldsymbol{r}) \qquad (1.34)$$

We can use this gauge condition and the identity

$$\nabla \times \nabla \times \boldsymbol{u} = -\nabla^2 \boldsymbol{u} + \nabla\left(\nabla \cdot \boldsymbol{u}\right), \qquad (1.35)$$

valid for any $\boldsymbol{u}$ to find, assuming harmonic fields, that

$$\left(\nabla^2 + k^2\right) \boldsymbol{A}(\boldsymbol{r}) = -\mu \boldsymbol{J}(\boldsymbol{r}) \tag{1.36}$$

We can now construct a scalar Green's function for the vector potential by solving for the case of a point source, i.e.

$$\left(\nabla^2 + k^2\right) G(\boldsymbol{r}, \boldsymbol{r}') = -\delta(\boldsymbol{r} - \boldsymbol{r}') \tag{1.37}$$

where $\boldsymbol{r}$ is the observation point and $\boldsymbol{r}'$ the position of a source, and δ the delta function. Using this G we calculate $\boldsymbol{A}$ by summing over all the individual sources

$$\boldsymbol{A}(\boldsymbol{r}) = \mu \int_V \boldsymbol{J}(\boldsymbol{r}') G(\boldsymbol{r}, \boldsymbol{r}') \mathrm{d}V' \tag{1.38}$$

For a point source $\boldsymbol{J}(\boldsymbol{r}) = (i\mu\omega)^{-1} \delta(\boldsymbol{r} - \boldsymbol{r}')\hat{\boldsymbol{x}}$ we find

$$\boldsymbol{A}(\boldsymbol{r}) = \frac{1}{i\omega} G(\boldsymbol{r}, \boldsymbol{r}')\hat{\boldsymbol{x}} \tag{1.39}$$

Using (1.31) and (1.32) we find

$$\boldsymbol{E}(\boldsymbol{r}) = i\omega \left[1 + \frac{1}{k^2}\nabla\nabla\cdot\right] \boldsymbol{A}(\boldsymbol{r}) \tag{1.40}$$

Returning to Maxwell's Equations we have the inhomogenous wave equation for the electromagnetic field

$$\nabla \times \nabla \times \boldsymbol{E}(\boldsymbol{r}) - k^2 \boldsymbol{E}(\boldsymbol{r}) = i\omega\mu \boldsymbol{J}(\boldsymbol{r}) \tag{1.41}$$

We can write a Dyadic Green's function solution to this wave equation as

$$\nabla \times \nabla \times \overleftrightarrow{G}(\boldsymbol{r}, \boldsymbol{r}') - k^2 \overleftrightarrow{G}(\boldsymbol{r}, \boldsymbol{r}') = \mathbb{1}_3 \delta(\boldsymbol{r} - \boldsymbol{r}') \tag{1.42}$$

where $\mathbb{1}_3 = \hat{\boldsymbol{x}} \otimes \hat{\boldsymbol{x}} + \hat{\boldsymbol{y}} \otimes \hat{\boldsymbol{y}} + \hat{\boldsymbol{z}} \otimes \hat{\boldsymbol{z}}$ is the 3-dimensional unit dyad. The connection between this Green's function and the field $\boldsymbol{E}$ is

$$\boldsymbol{E}(\boldsymbol{r}) = \boldsymbol{E}_0(\boldsymbol{r}) + i\omega \int_V \overleftrightarrow{G}(\boldsymbol{r}, \boldsymbol{r}') \cdot \boldsymbol{J}(\boldsymbol{r}') \mathrm{d}V' \tag{1.43}$$

where $\boldsymbol{E}_0(\boldsymbol{r})$ is a solution to (1.41) when $\boldsymbol{J} = 0$. Similarly we can write an equation for $\boldsymbol{H}(\boldsymbol{r})$

$$\boldsymbol{H}(\boldsymbol{r}) = \boldsymbol{H}_0(\boldsymbol{r}) + \int_V \left[\nabla \times \overleftrightarrow{G}(\boldsymbol{r}, \boldsymbol{r}')\right] \cdot \boldsymbol{J}(\boldsymbol{r}') \mathrm{d}V' \tag{1.44}$$

Comparing the Green's functions for $\boldsymbol{E}(\boldsymbol{r})$ and $\boldsymbol{A}(\boldsymbol{r})$, we find

$$\overleftrightarrow{G}(\boldsymbol{r}, \boldsymbol{r}') = \mathcal{D} G(\boldsymbol{r}, \boldsymbol{r}') \tag{1.45}$$

$$\mathcal{D} := \mathbb{1}_3 + \frac{1}{k^2} \nabla\nabla \tag{1.46}$$

Once we have the Dyadic Green's function, we can calculate the spontaneous emission rate of a dipole emitter at position $\boldsymbol{r}_i$ with dipole moment $\boldsymbol{\mu}_i$ as [22, 32]

$$\Gamma_{tot} = \frac{2\omega_0^2}{\epsilon_0 c^2 \hbar} \mathrm{Im} \left[\boldsymbol{\mu}_i^* \cdot \overleftrightarrow{G}(\omega_0, \boldsymbol{r}_i, \boldsymbol{r}_i) \cdot \boldsymbol{\mu_i}\right] \tag{1.47}$$

As expected, the total emission is proportional to the electromagnetic field.

1.4 Outline of thesis

In the present chapter we outlined key physical and mathematical concepts that will serve as a framework for the subsequent parts of this thesis. In chapter 2 we use the quasi-static approximation and examine the radiative enhancement of a multi-layer concentric cylinder structure. These results provide intuition into the results of chapter 3, where we experimentally and numerically investigate plasmonic enhancement of an InGaN single photon source in a truncated pillar structure. In chapter 4 we will look at the role dimension plays in the properties of cooperative light scattering phenomenon, that serve as the precursor to important experimentally observable phenomena such as superradiance. In chapter 5, we will apply the theory of the previous chapter to obtain signatures of superradiance in the minimally studied two dimensional case. We will also examine the interplay between the photon mediated cooperative coupling between atoms and the dressing of individual atoms with a strong driving laser field.

CHAPTER II

Radiative enhancement of cylindrical nano-pillar: theory

In this section we analytically explore how metal and dielectric coatings change the spontaneous emission of an infinite dielectric cylinder. Multi-layer cylinders, spheres, and planar slabs have all been the subject of considerable study. We will review some of the previous work to understand how dielectric coatings change the spontaneous emission rate, and present our own simple analytic formula for how the spontaneous emission rate is changed in the context of the quasi-static approximation.

2.1 Slabs and Mirrors

It was predicted theoretically [60, 10] and shown experimentally [21] that the spontaneous emission of molecules near a perfectly conducting mirror was oscillatory dependent upon the distance to the mirror. Such a perfectly conducting mirror could be treated by the method of images, where the result is due to the fact that the electromagnetic field of one emitter effects that of the other by modification of the electromagnetic environment. Later authors realized that further improvements could be made using multi-layer structures, and formed cavities using planar distributed bragg reflector (DBR) mirrors [85]. By using metal/dielectric alternating layers, enhancement by of the spontaneous emission rate by hyperbolic metamaterials has been considered, which yielded broadband purcell enhancement [38].

2.2 Spheres

Inside a nanosphere of dielectric constant ϵ_1 with surrounding medium described by dielectric ϵ_2 we have an enhancement of the spotaneous emission rate compared to when the nanosphere is not present [12]

$$\frac{\Gamma}{\Gamma_0} = \left(\frac{3}{2 + \epsilon_1/\epsilon_2}\right)^2 \tag{2.1}$$

Study has also been done on the multi-layered sphere case, with a derivation of a complicated expression for the dyadic Green's function for a multi-layered spherical structure [51]. When alternating metal and dielectric layers are used, hyperbolic metamaterials can be constructed, and these structures have been studied with the goal of optical cloaking [46].

2.3 Cylinders

Previous work has been done investigating spontaneous emission near for an emitter near a cylindrical structure [44, 11] in the quasistatic approximation. Dyadic Green's functions have also been thoroughly investigated in the cylindrical geometry. For the case of a photonic crystal made of cylinders, the dyadic Green's function found in [30] shows that the local density of states, proportional to the spontaneous emission rate, can be manipulated by an order of magnitude. We also have dyadic Green's function for multi-layered cylindrical structures [50] that can be used to calculate the spontaneous emission rate.

2.4 Analytic infinite nano-cylinder

In this section we will derive results for the change in spontaneous emission rate for a dipole emitter embedded in a multi-latyer nano-cylinder with different dielectric constants for each later. We will use this structure to provide intuition to compare to theoretical and simulation results for a truncated cylinder [18]. Our treatment follows that of [11], but considers the case of a dipole embedded inside the cylinder, and also extends the results to the case of multiple concentric cylinders with different dielectric constants.

2.4.1 Two dielectric regions

We consider an infinite dielectric cylinder of radius R with possibly complex dielectric constant ϵ_1 surrounded by a media of dilectric constant ϵ_2. We will consider a point charge at position ρ' and solve for the field at position ρ. Poisson's equation for a point charge in this case gives

$$\nabla^2 g(\boldsymbol{r}, \boldsymbol{r}') = -\frac{4\pi}{\rho}\delta(\rho - \rho')\delta(\phi - \phi')\delta(z - z') \tag{2.2}$$

Using [44, 11] we can expand the delta function in cylindrical coordinates

$$\delta(z - z') = \frac{1}{\pi}\int_0^\infty \mathrm{d}k \cos k(z - z') \tag{2.3}$$

$$\delta(\phi - \phi') = \frac{1}{2\pi}\sum_{m=0}^{\infty}(2 - \delta_{m0})\cos m(\phi - \phi') \tag{2.4}$$

which allows us to write $g(\boldsymbol{r}, \boldsymbol{r}')$ as

$$g(\boldsymbol{r}, \boldsymbol{r}') = \frac{1}{2\pi^2}\sum_{m=0}^{\infty}\int_0^\infty (2 - \delta_{m0})\cos m(\phi - \phi')\cos k(z - z') g_m(k, \rho, \rho'), \tag{2.5}$$

where the radial component of the green's function $g_m(k, \rho, \rho')$ satisfies Bessel's equation

$$\frac{1}{\rho}\partial_\rho\left(\rho\partial_\rho g_m\right) - \left(k^2 + \frac{m^2}{\rho^2}\right) g_m = -\frac{4\pi}{\rho}\delta(\rho - \rho') \tag{2.6}$$

The two linearly independent solutions to (2.6) are the modified Bessel functions $I_m(k\rho)$ and $K_m(k\rho)$. We consider the form of g_m in regions $\rho < \rho' < R$, $\rho' < \rho < R$ and $\rho > R$ respectively, and find for $\rho < R$ by symmetry we have

$$g_m(k, \rho, \rho') = I_m(k\rho_<)[K_m(k\rho_>) + A_{m,1}(k)I_m(k\rho_>)] \tag{2.7}$$

Where $A_{m,1}$ is a function of k to be determined by boundary conditions and $\rho_<(\rho_>)$ is the lesser(greater) of ρ an ρ'. For $\rho > R$ we wish to avoid the divergence at $\rho = \infty$ so we have

$$g_m(k, \rho, \rho') = A_{m,2}(k)K_m(k\rho) \tag{2.8}$$

To get the overall normalization correct, we note that when $\epsilon_1 = \epsilon_2$ we recover the case of a dipole in free space, which gives

$$\begin{aligned} g(\boldsymbol{r}, \boldsymbol{r'}) =& \frac{1}{4\pi\epsilon_1|\boldsymbol{r} - \boldsymbol{r'}|} \\ =& \frac{1}{2\pi^2\epsilon_1}\sum_{m=0}^{\infty}(2 - \delta_{m0})\cos m(\phi - \phi')\int_0^\infty \cos k(z - z')K_m(k\rho_>)I_m(k\rho_<) \end{aligned} \tag{2.9}$$

Comparing to this solution, we must have that for $\epsilon_1 \neq \epsilon_2$ and $\rho < R$

$$\begin{aligned} g(\boldsymbol{r}, \boldsymbol{r'}) =& \frac{1}{2\pi^2\epsilon_1}\sum_{m=0}^{\infty}(2 - \delta_{m0})\cos m(\phi - \phi') \\ & \times\int_0^\infty \cos k(z - z')I_m(k\rho_<)[K_m(k\rho_>) + A_{m,1}(k)I_m(k\rho_>)], \end{aligned} \tag{2.10}$$

and for $\rho > R$

$$
\begin{aligned}
g(\boldsymbol{r},\boldsymbol{r}') =& \frac{\epsilon}{2\pi^2\epsilon_1}\sum_{m=0}^{\infty}(2-\delta_{m0})\cos m(\phi-\phi') \\
&\times\int_0^{\infty}\cos k(z-z')A_{m,2}(k)I_m(k\rho')K_m(k\rho). \qquad (2.11)
\end{aligned}
$$

Here $\epsilon = \epsilon_1/\epsilon_2$.

2.4.1.1 Radiative enhancement

We can find the unknowns $A_{m,1}(k)$ and $A_{m,2}(k)$ by imposing boundary conditions: i) continuity of the field, ii) continuity of the displacement field, which is continuity of normal derivative multiplied by the dielectric permittivity. Solving we find

$$
\begin{aligned}
A_{m,1}(k) =& \frac{(\epsilon-1)K_m(kR)'K_m(kR)}{I_m(kR)K_m(kR)'-\epsilon I_m(kR)'K_m(kR)}, \qquad (2.12)\\
A_{m,2}(k) =& \frac{I_m(kR)K_m(kR)'-I_m(kR)'K_m(kR)}{I_m(kR)K_m(kR)'-\epsilon I_m(kR)'K_m(kR)}. \qquad (2.13)
\end{aligned}
$$

The $'$ denotes a derivative with respect to the function argument $\frac{\partial}{\partial(k\rho)}$. The $m = 1$ term is the dipole term which will provide the dominant contribution to the far-field emission. The integrands involving Bessel functions fall off exponentially for $\rho \ll \rho'$ and so we can take the small argument approximation of the bessel functions valid for $m \geq 1$ (cite)

$$
\begin{aligned}
I_m(x) \to& \frac{1}{\Gamma(m+1)}\left(\frac{x}{2}\right)^m \qquad (2.14)\\
K_m(x) \to& \frac{\Gamma(m)}{2}\left(\frac{2}{x}\right)^m \qquad (2.15)
\end{aligned}
$$

For the purpose of finding radiative enhancement in the far-field we are interested in $A_{1,2}(k)$,

$$A_{1,2}(k) \approx \frac{2}{1+\epsilon} \tag{2.16}$$

which gives radiative enhancement of a radial dipole

$$\left(\frac{\Gamma_{\mathrm{rad}}}{\Gamma_0}\right)_\rho = |A_{1,2}(k)|^2 = \left|\frac{2\epsilon_1}{\epsilon_1+\epsilon_2}\right|^2 \tag{2.17}$$

2.4.1.2 Nonradiative decay

As shown by Fermi's golden rule, the transition rate between states is proportional to the density of modes, which is in turn proportional to the electromagnetic field. The nonradiative decay is proportional to the losses in the near-field, which is given by the nonradiative part of the electric field. From [11] we have that

$$\left(\frac{\Gamma_{\mathrm{nr}}}{\Gamma_0}\right)_\rho \approx \frac{6\pi\epsilon_0}{k_0^3\sqrt{\epsilon_1}}\frac{\mathrm{Im}\hat{\boldsymbol{\rho}}\cdot\boldsymbol{E}(\boldsymbol{\rho}',\boldsymbol{\rho}')}{|\boldsymbol{d}_0|}, \tag{2.18}$$

We find that for a dipole located inside the inner cylinder (as opposed to outside as considered by [11]) that the decay is then

$$\left(\frac{\Gamma_{\mathrm{nr}}}{\Gamma_0}\right)_\rho \approx \frac{6}{\pi k_0^3\sqrt{\epsilon_1}}\sum_{m=1}^{\infty}\int_0^\infty \mathrm{d}k k^2\left[I_m(k\rho')^{'}\right]^2 \mathrm{Im}A_{m,1}(k), \tag{2.19}$$

$$:= \frac{6}{\pi k_0^3\sqrt{\epsilon_1}}\sum_{m=1}^{\infty}\int_0^\infty \mathrm{d}k l_m(k,\rho',R_1). \tag{2.20}$$

The function $A_{m,1}(k)$ can be found using Cramer's rule. The challenge is finding the nonradiative decay rate analytically is infinitely many m terms contribute, unlike the far-field which is dominated by the $m = 1$ term. Furthermore, both large and small

k contribute to the result, and we find

$$l_m(k,\rho',R_1) \approx \begin{cases} \frac{m}{2\rho'^2\epsilon_1}\mathrm{Im}\left(\frac{\epsilon_1-\epsilon_2}{\epsilon_1+\epsilon_2}\right)\left(\frac{\rho'}{R_1}\right)^{2m} & k\to 0 \\ \frac{k}{2R_1\epsilon_1}\mathrm{Im}\left(\frac{\epsilon_1-\epsilon_2}{\epsilon_1+\epsilon_2}\right)e^{-2k(R_1-\rho')} & k\to\infty \end{cases} \tag{2.21}$$

This is the same result as found by [11] for a dipole outside a wire but with the roles of ρ' and R_1 switched and the roles of the dielectrics switched. Following that treatment we model l_m as a Lorentzian

$$l_m \approx \frac{\frac{m}{2\rho'^2\epsilon_1}\mathrm{Im}\left(\frac{\epsilon_1-\epsilon_2}{\epsilon_1+\epsilon_2}\right)\left(\frac{\rho'}{R_1}\right)^{2m}}{1+k^2(R_1-\rho')^2} \tag{2.22}$$

This allows the integration to be performed exactly, yielding

$$\left(\frac{\Gamma_{\mathrm{nr}}}{\Gamma_0}\right)_\rho \approx \frac{3}{16k_0^3(R_1-\rho')^3\epsilon_1^{3/2}}\mathrm{Im}\left(\frac{\epsilon_1-\epsilon_2}{\epsilon_1+\epsilon_2}\right) \tag{2.23}$$

2.4.2 Three dielectric regions

We consider the case of an infinite cylinder of radius R_1 and dielectric constant ϵ_1 for $\rho < R_1$ concentrically embedded in a dielectric cylinder with outer radius R_2 and dielectric constant ϵ_2 for $R_1 < \rho < R_2$. For $\rho > R_2$ this infinite cylinder is in a media with permittivity ϵ_3. The situation is analogous to the previous 2-dielectric region infinite cylinder case, with the key ingredient being to solve for the radial Green's function $g_m(k,\rho,\rho')$. We find that

$$g_m(k,\rho,\rho') = I_m(k\rho_<)\left[K(k\rho_>) + A_{m,1}(k)I_m(k\rho_>)\right] \qquad 0<\rho<R_1 \tag{2.24}$$

$$g_m(k,\rho,\rho') = I_m(k\rho')\left[A_{m,2}(k)K_m(k\rho) + A_{m,3}(k)I_m(k\rho)\right] \qquad R_1<\rho<R_2 \tag{2.25}$$

$$g_m(k,\rho,\rho') = I_m(k\rho')\left[A_{m,4}(k)K_m(k\rho)\right] \qquad \rho>R_2 \tag{2.26}$$

These equations have 4 unknowns $A_m(k), B_m(k), C_m(k), D_m(k)$ but also 4 boundary condition equations: the continuity of the displacement field and g_m itself. We can write the equations in matrix form $Mx = y$ with

$$M = \begin{bmatrix} I_{R_1} & -K_{R_1} & -I_{R_1} & 0 \\ \epsilon_1 I'_{R_1} & -\epsilon_2 K'_{R_1} & \epsilon_2 I'_{R_1} & 0 \\ 0 & K_{R_2} & I_{R_2} & -K_{R_2} \\ 0 & \epsilon_2 K'_{R_2} & \epsilon_2 I'_{R_2} & -\epsilon_3 K'_{R_2} \end{bmatrix} \quad x = \begin{bmatrix} A_1 \\ A_2 \\ A_3 \\ A_4 \end{bmatrix} \quad y = \begin{bmatrix} -K_{R_1} \\ -\epsilon_1 K'_{R_1} \\ 0 \\ 0 \end{bmatrix} \tag{2.27}$$

Here we have employed the notation

$$I_\alpha = I_m(k\alpha) \tag{2.28}$$

$$K_\alpha = K_m(k\alpha) \tag{2.29}$$

$$A_{m,i}(k) = A_i \tag{2.30}$$

The far field, which determines radiative enhancement, is given by $|A_{1,4}(k)|^2$. To find A_4 we employ Cramer's rule,

$$x_i = \frac{\det(M_i)}{\det M}, \tag{2.31}$$

where M_i is the matrix formed by replacing the i^{th} column of M by y. Taking the small argument form of the Bessel functions valid in the far-field and taking the $m = 1$ dipole term, we find

$$\det\left(M^{(m=1)}\right) \rightarrow \frac{R_1^2(\epsilon_1 - \epsilon_2)(\epsilon_2 - \epsilon_3) + R_2^2(\epsilon_1 + \epsilon_2)(\epsilon_2 + \epsilon_3)}{4R_1R_2^3} \tag{2.32}$$

$$\det\left(M_4^{(m=1)}\right) \rightarrow \frac{\epsilon_1\epsilon_2}{R_1R_2} \tag{2.33}$$

We then find the radiative enhancement as

$$\left(\frac{\Gamma_{\text{rad}}}{\Gamma_0}\right)_\rho = |A_{1,4}(k)|^2 = \left|\frac{4\epsilon_1\epsilon_2}{(\epsilon_1+\epsilon_2)(\epsilon_2+\epsilon_3)+(R_1^2/R_2^2)\,(\epsilon_1-\epsilon_2)(\epsilon_2-\epsilon_3)}\right|^2 \tag{2.34}$$

We note the potential for an even stronger resonance than in the 2-dielectric region case when $\epsilon_1 \approx -\epsilon_2 \approx \epsilon_3$ and $R_1 \ll R_2 \ll \lambda$.

2.4.3 Four dielectric regions

We consider the case of three concentric cylinders of radii R_1, R_2, R_3 dividing space into 4 dielectric regions of constant dielectric constants $\epsilon_1, \epsilon_2, \epsilon_3, \epsilon_4$. As in the 2- and 3-dielectric region cases, we can write the radial component of the green's function in the 4 regions

$$g_m(k,\rho,\rho') = I[A_{2i-2}K + A_{2i-1}I] \qquad R_{i-1} < \rho < R_i \qquad i \in \{1,2,3,4\}. \tag{2.35}$$

Here, the arguments of the Bessel functions I and K are understood, and $A_0 := 1, A_7 := 0, R_0 := 0, R_4 := \infty$. At the three boundaries between dielectric regions there are 2-boundary condition equations each, resulting in 6 equations total. Using the notation where the arguments of the Bessel functions are understood, we have

$$\begin{bmatrix} I & -K & -I & 0 & 0 & 0 \\ \epsilon_1 I' & -\epsilon_2 K' & -\epsilon_2 I' & 0 & 0 & 0 \\ 0 & K & I & -K & -I & 0 \\ 0 & \epsilon_2 K' & \epsilon_2 I' & -\epsilon_3 K' & -\epsilon_3 I' & 0 \\ 0 & 0 & 0 & K & I & -K \\ 0 & 0 & 0 & \epsilon_3 K' & \epsilon_3 I' & -\epsilon_4 K' \end{bmatrix} \begin{bmatrix} A_1 \\ A_2 \\ A_3 \\ A_4 \\ A_5 \\ A_6 \end{bmatrix} = \begin{bmatrix} -K \\ -\epsilon_1 K' \\ 0 \\ 0 \\ 0 \\ 0 \end{bmatrix} \tag{2.36}$$

Employing the small argument limit of the Bessel functions are looking at the

$m = 1$ dipole term we have

$$\begin{aligned}\det\left(M^{(m=1)}\right) =& \frac{1}{(2R_1R_2R_3)^3}\Big(R_1^2R_2^2R_3^2(\epsilon_1+\epsilon_2)(\epsilon_2+\epsilon_3)(\epsilon_3+\epsilon_4)\\ &+R_1^4R_2^2(\epsilon_1-\epsilon_2)(\epsilon_2+\epsilon_3)(\epsilon_3-\epsilon_4)+R_1^4R_3^2(\epsilon_1-\epsilon_2)(\epsilon_2-\epsilon_3)(\epsilon_3+\epsilon_4)\\ &+R_1^2R_2^4(\epsilon_1+\epsilon_2)(\epsilon_2-\epsilon_3)(\epsilon_3-\epsilon_4)\Big) \qquad (2.37)\\ \det\left(M_6^{(m=1)}\right) =& \frac{\epsilon_1\epsilon_2\epsilon_3}{R_1R_2R_3} \qquad (2.38)\end{aligned}$$

This gives a radiative enhancement in the far-field of

$$\left(\frac{\Gamma_{\text{rad}}}{\Gamma_0}\right)_\rho = \left|\frac{2^3\epsilon_1\epsilon_2\epsilon_3}{\epsilon_{12}^+\epsilon_{23}^+\epsilon_{34}^+ + \epsilon_{12}^-\epsilon_{23}^-\epsilon_{34}^+(R_1/R_2)^2 + \epsilon_{12}^-\epsilon_{23}^+\epsilon_{34}^-(R_1/R_3)^2 + \epsilon_{12}^+\epsilon_{23}^-\epsilon_{34}^-(R_2/R_3)^2}\right|^2 \qquad (2.39)$$

$$\epsilon_{ij}^\pm = \epsilon_i \pm \epsilon_j \qquad (2.40)$$

2.4.4 N dieletric regions

2.4.4.1 Radiative decay

Here we consider the general case of $N-1$ concentric cylinders of radii R_i, $i \in \{1,\dots,N-1\}$ dividing space in to N dielectric regions ϵ_j, $j \in \{1,\dots,N\}$. As before, the critical piece for determining the radiative enhancement is the radial component of the scalar dyadic green's function, which in each of the N regions is given by

$$g_m(k,\rho,\rho') = I[A_{2i-2}K + A_{2i-1}I] \qquad R_{i-1} < \rho < R_i \qquad i \in \{1,\dots,N\}, \qquad (2.41)$$

where $A_0 := 1$, $A_{2N-1} := 0$ and $R_0 = 0$, $R_N = \infty$. There are $N-1$ boundaries between the N dielectric regions, at at each region boundary we require continuity of g_m and continuity of the normal derviative of g_m times the dielectric permittivity, giving $2N-2$ total boundary condition equations. These equations can then be solved via Cramer's rule. The result is

$$\frac{\Gamma_{\text{rad}}}{\Gamma_0} = \left| \frac{a}{b_+(m=1)} \right|^2, \tag{2.42}$$

$$a = \prod_{i=1}^{N-1} (2\epsilon_i), \tag{2.43}$$

$$b_\pm = \sum_{\alpha_1 \in \{-1,1\}} \cdots \sum_{\alpha_{N-1} \in \{-1,1\}} f_\pm g h_\pm, \tag{2.44}$$

$$f_\pm(\alpha_1, \ldots, \alpha_{N-1}) = \frac{1}{2} \left(1 \pm \prod_{i=1}^{N-1} \alpha_i \right), \tag{2.45}$$

$$g\left(\alpha_1, \ldots, \alpha_{N-1}\right) = \prod_{i=1}^{N-1} \left(\epsilon_i + \alpha_i \epsilon_{i+1}\right), \tag{2.46}$$

$$h_\pm\left(\alpha_1, \ldots, \alpha_{N-1}, R_1, \ldots R_{N-1}, m\right) = (R_1)^{m\alpha_1(\alpha_1 \mp 1)} \prod_{i=2}^{N-1} \left(R_i^{\pm m \alpha_1 (\alpha_i - 1) \prod_{j=2}^{i} \alpha_j} \right). \tag{2.47}$$

There are 2^{N-1} terms in the $N-1$ sums over ±1. Half of those terms vanish, as the function $f = 1$ when the product of all the signs is positive and $f = 0$ otherwise, so there are 2^{N-2} nonzero terms. Each term is made up of the product of $N-1$ sums or differences of adjacent dielectrics given by the function g. The function h describes the appearance of the radii, and only for $\alpha_i = 1$ does R_i appear, so a given R_i will appear in 2^{N-3} terms of b for $N \geq 3$. Note that b_- is the same as b_+ but with the replacements $\epsilon_{12}^{\pm} \to \epsilon_{12}^{\mp}$. As an example, for $N = 5$ we have

$$\begin{aligned} b_\pm = & \epsilon_{12}^{\pm}\epsilon_{23}^{+}\epsilon_{34}^{+}\epsilon_{45}^{+} + \epsilon_{12}^{\mp}\epsilon_{23}^{-}\epsilon_{34}^{+}\epsilon_{45}^{+} \left(\frac{R_1}{R_2}\right)^{2m} + \epsilon_{12}^{\mp}\epsilon_{23}^{+}\epsilon_{34}^{-}\epsilon_{45}^{+} \left(\frac{R_1}{R_3}\right)^{2m} \\ & + \epsilon_{12}^{\mp}\epsilon_{23}^{+}\epsilon_{34}^{+}\epsilon_{45}^{-} \left(\frac{R_1}{R_4}\right)^{2m} + \epsilon_{12}^{\pm}\epsilon_{23}^{-}\epsilon_{34}^{-}\epsilon_{45}^{+} \left(\frac{R_2}{R_3}\right)^{2m} + \epsilon_{12}^{\pm}\epsilon_{23}^{-}\epsilon_{34}^{+}\epsilon_{45}^{-} \left(\frac{R_2}{R_4}\right)^{2m} \\ & + \epsilon_{12}^{\pm}\epsilon_{23}^{+}\epsilon_{34}^{-}\epsilon_{45}^{-} \left(\frac{R_3}{R_4}\right)^{2m} + \epsilon_{12}^{\mp}\epsilon_{23}^{-}\epsilon_{34}^{-}\epsilon_{45}^{-} \left(\frac{R_1 R_3}{R_2 R_4}\right)^{2m} \end{aligned} \tag{2.48}$$

2.4.4.2 Nonradiative decay

The determinant of the $(2N-2)\times(2N-2)$ matrix M of from the boundary conditions at the $N-1$ dielectric interfaces is given by

$$\det M^{(m)} = \frac{b_+}{\prod_{i=1}^{N-1}(2R_i)} \tag{2.49}$$

To solve for $A_{m,1}$ we also need

$$\det M_1^{(m)} = \frac{2^{2m-N}\Gamma(m+1)\Gamma(m)}{(kR_1)^{2m}} \frac{b_-}{\prod_{i=1}^{N-1} R_i} \tag{2.50}$$

This allows us to write

$$A_{m,1} = \frac{\det M_1^{(m)}}{\det M^{(m)}} = \frac{2^{2m-1}\Gamma(m)\Gamma(m+1)}{(kR_1)^{2m}} \frac{b_-}{b_+} \tag{2.51}$$

which gives

$$\begin{aligned}\left(\frac{\Gamma_{\text{nr}}}{\Gamma_0}\right)_\rho =& \frac{6}{\pi k_0^3\sqrt{\epsilon_1}} \sum_{m=1}^{\infty}\int_0^{\infty} \mathrm{d}k l_m(k,\rho',R_1,\ldots,R_{N-1}) \\ l_m(k,\rho',R_1,\ldots,R_{N-1}) =& \frac{m}{2\rho'^2}\left(\frac{\rho'}{R_1}\right)^{2m} \operatorname{Im}\left(\frac{b_-}{b_+}\right) \qquad k\to 0\end{aligned} \tag{2.52}$$

The $k\to\infty$ behavior of l_m can be found using $\operatorname{Im}\left(\frac{b_-(e^{2kR_1/m},\ldots,e^{2kR_{N-1}/m})}{b_+(e^{2kR_1/m},\ldots,e^{2kR_{N-1}/m})}\right)$ instead of $\operatorname{Im}\left(\frac{b_-(R_1,\ldots,R_{N-1})}{b_+(R_1,\ldots,R_{N-1})}\right)$. Since b_+ and b_- are dependent on m for $N\geq 2$ it becomes difficult to write a simple analytic expression for the non-radiative decay rate in the general case.

2.5 Application of quasi-static theory

We now apply the results of our analytic cylinder theory to a realistic experimental geometry. In our experiments we have a GaN based core, which we surround with an Al_2O_3 spacer layer and then coat with Ag for plasmonic enhancement. We find that the maximum radiative enhancement is proportional to the ratio of the real to imaginary part of the dielectric constant of the metal when it is on resonance with a real dielectric,

$$\left(\frac{\Gamma_{\text{rad}}}{\Gamma_0}\right)_{\rho,max} \propto \left|\frac{\text{Re}(\epsilon_{Ag})}{\text{Im}(\epsilon_{Ag})}\right|^2 . \tag{2.53}$$

The width of the resonance is proportional to $\text{Im}(\epsilon_{Ag})$ and the wavelength of the resonance is given by $\text{Re}(\epsilon_{Ag})$. For plasmonic structures with Gan and silver, applying (1.17) the quasistatic approximation is quite accurate for $R_{\text{max}} < 11nm$ and remains a valid approximation for

$$R_{\text{max}} < 28nm \tag{2.54}$$

This requirement is not met by the nanostructures we consider here, as it is difficult to make multilayer structures with such small size. From Fig. 2.1 we see the maximum enhancement is obtained around $R_{\text{max}} \approx 52nm$ (which assumes the quasistatic approximation). However, from (2.42) we have the scaling property

$$\left(\frac{\Gamma_{\text{rad}}}{\Gamma_0}\right)_{\rho}(\alpha R_1, \ldots, \alpha R_{N-1}) = \left(\frac{\Gamma_{\text{rad}}}{\Gamma_0}\right)_{\rho}(R_1, \ldots, R_{N-1}) . \tag{2.55}$$

So, if we scale all radii by the same factor, the quasistatic approximation predicts the same radiative enhancement, and this by scaling the structure small enough the approximation will eventually become valid. However, as the size of the structure is reduced, the non-radiative decay processes become enhanced as the lossy metal layer comes closer to the emitter. From (2.23) and (2.52) we see

$$\left(\frac{\Gamma_{\text{nr}}}{\Gamma_0}\right)_{\rho}(\alpha R_1, \ldots, \alpha R_{N-1}) \approx \frac{1}{\alpha^3}\left(\frac{\Gamma_{\text{nr}}}{\Gamma_0}\right)_{\rho}(R_1, \ldots, R_{N-1}) \tag{2.56}$$

The different scaling behavior of the radiative and non-radiative enhancement suggest the usefulness of a dielectric spacer layer, which will reduce the non-radiative recombination while having a smaller effect on the radiative rate.

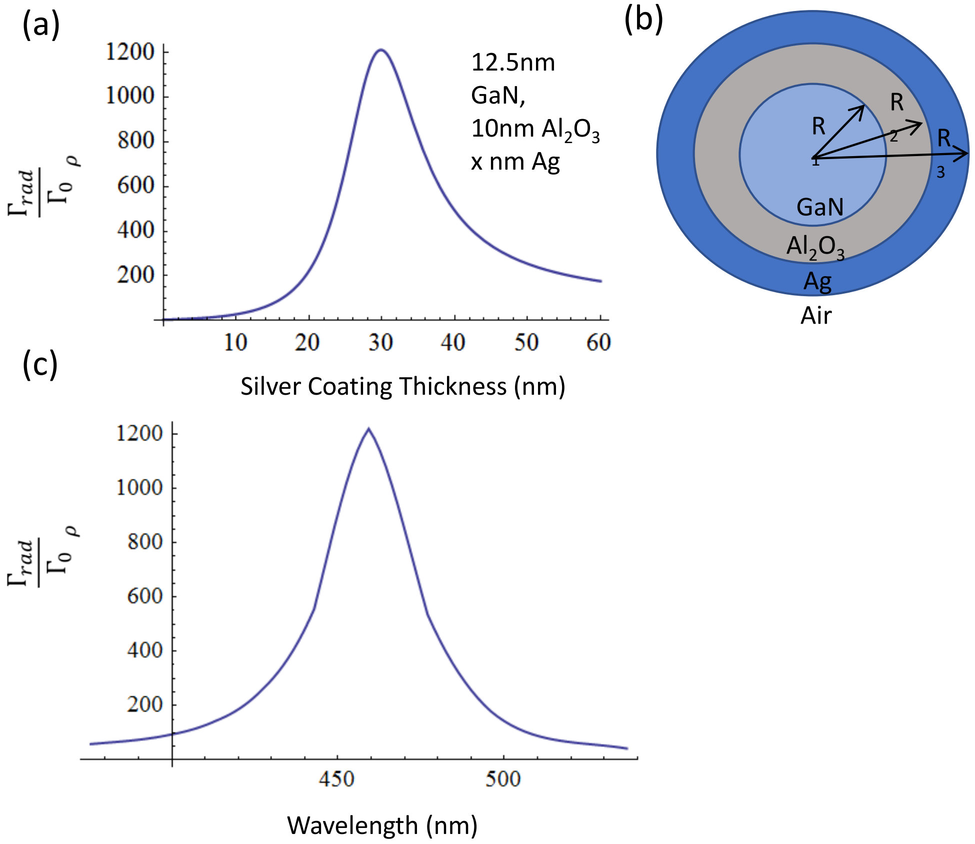

Figure 2.1: (a) The plot shows the radiative enhancement $(\Gamma_{\text{rad}}/\Gamma_0)_\rho$ for a 25nm GaN pillar with dielectric constant $\epsilon_{GaN} = 6.27$ surrounded by a 10 nm thick layer of Al_2O_3 with dielectric constant $\epsilon_{\text{Al}_2\text{O}_3} = 3.17$ sounded by a variable thickness coating of silver with dielectric constant $\epsilon_{Ag} = -6.27 + 0.20i$ at 435 nm surrounded by air, $\epsilon_{\text{air}} = 1.$ (b) shows the cross-sectional view of the concentric cylinders with variable dielectric coatings, labeling R_1, R_2, R_3 used in the theory. In (c) we caclulate the enhancement as a function of wavelength for 12.5nm GaN, 10nm Al_2O_3 and 30nm Ag using GaN data from [3] and Ag data from [41]

CHAPTER III

Plasmonic enhancement of quantum dot-in-pillar: experiment

In this section we aim to demonstrate plasmonic enhancement of the intensity and radiative emission rate of size- and site-controlled InGaN quantum dots. Our methodology is simple - encapsulate the pillar-like structure of the quantum dots in a layer of silver, which gives broadband enhancement of the photoluminescence. The work in this chapter was done is close collaboration with Brandon Demory from Associate Professor P.C. Ku's group in the EECS department at the university of Michigan. Brandon carried out the simulation and fabrication, whereas I carried out optical measurements. Both authors contributed to the analysis, with author contributions as shown in [18].

3.1 Introuction

Epitaxial quantum dots have the potential to serve as rapid emitters of single photon, as compared to atoms [9], molecules [54], colloidal quantum dots [8, 17], and vacancy-centers in diamond [39]. Gallium Nitride quantum dots are of particular interest due to their potential for non-cryogenic operation temperatures [42, 37].

Radiative enhancement can be accomplished in III-V quantum dots by coupling

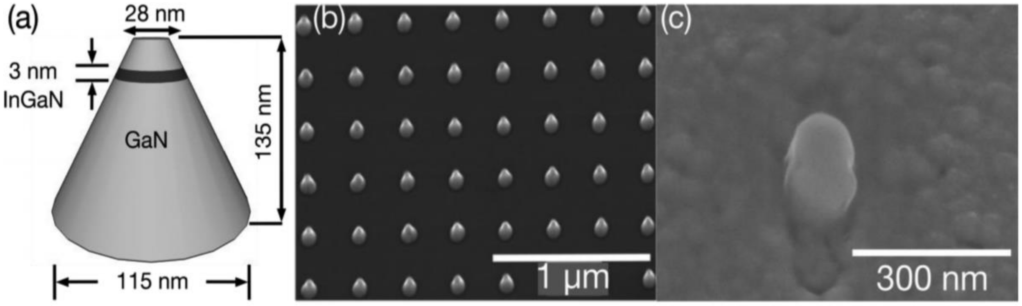

Figure 3.1: (a) geometry of an individual quantum dot, which consists of a 3nm InGaN disk embedded in a GaN pillar created via inductively coupled plasma reactive ion etching (ICP-RIE) (b) a regular array of QD with subwavelength spacing (c) SEM image of an individual dot. Figure from [18]

to photonic crystals [66, 34, 81] and plasmonic cavities [1, 69, 36]. In each case, the emission enhancement is governed by the Purcell effect, which is proportional to Q/V (1.2) Photonic crystals can have very high Q but due to the diffraction limit the mode volume V cannot go below the cubic wavelength. On the other hand, plasmonic cavities have relatively small $Q \sim \mathcal{O}(10)$ but the metal allows for very tight confinement of the modes and so small V. Due to the inhomogeneity present in quantum dots, we adopt the plasmonic coupling approach which enables broadband enhancement and easier fabrication [13].

3.2 Quantum dot properties

Details of the quantum dot fabrication can be found in [48] and extensive review of their optical properties in [88, 87]. The sample is shown in Fig. 3.1, it is located at the tip of a truncated cylinder. Once coated with a conformal layer of silver, this allows very tight confinement of the field near the active dot region. By employing a conformal layer of silver, we can simultaneously enhance an entire grid of quantum dots, as outlined in Fig. 3.1(b).

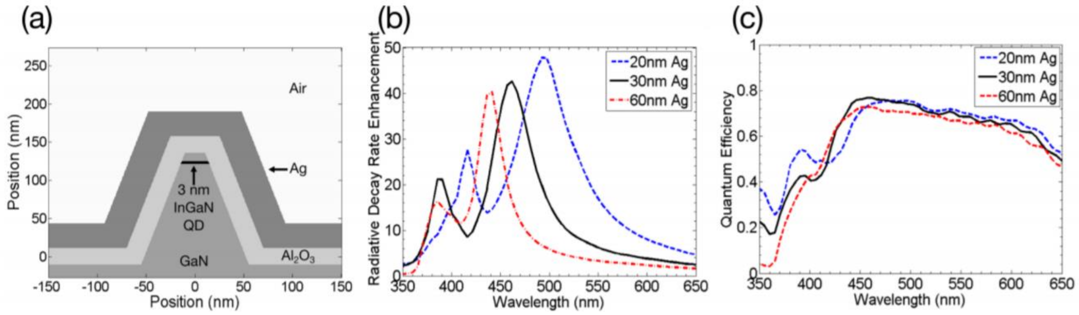

Figure 3.2: Taken from [18]. (a) gives a schematic of the structue (b) shows the radiative enhancement as a function of wavelength for varying Ag thickness. (c) gives the quantum efficiency.

3.3 Simulation of quantum dot enhancement

The result is two plasmon resonances, the greater of which gives radiative enhancement of approximately 50 as shown in Fig. 3.2(b). The nature of the multiple resonances is explained in [64] as a result of plasmon hybridization: the high energy resonance is between the InGaN and Al_2O_3 interface, whereas the lower energy resonance is across the Al_2O_3 shell. As silver thickness is increase, the resonances converge to the single resonance that would result from a metallic void. Numerical simulations in Fig. 3.2(c) show that the quantum efficiency

$$\mathrm{QE} = \frac{\Gamma_{\mathrm{rad}}}{\Gamma_{\mathrm{nr}} + \Gamma_{\mathrm{rad}}} \tag{3.1}$$

remains relatively high across the entire broadband low energy resonance. The position and Q value of the resonance are reasonably predicted by the crude quasistatic approximation.

3.4 Experimental results of quantum dot plasmonic enhancement

We perform photoluminescence (PL), time-resolved photoluminescence (TRPL), and second order correlation ($g^{(2)}$) measurements on the quantum dot samples before and after the deposition of silver. Details of the measurements can be found in [18]. The goal is to show enhanced PL intensity, which indicates that the radiative enhancement overcomes the metal losses, with more rapid emission of photons, and maintenance of the single photon properties.

From Fig. 3.3(f) we see that the quantum dot maintains its single photon source properties after the addition of the plasmonic cavity. Both the $g^{(2)}$ dip in Fig. 3.3(e),(f) and the time-resolved photoluminescence in Fig. 3.3(c),(d) show an order of magnitude reduction in the emission rate with the addition of Ag. We verify that this reduction in decay rate is mostly radiative as predicted by a simulated quantum efficiency of ≈ 0.7 by demonstrating enhancement of the photoluminescence in Fig. 3.3(a),(b). The photoluminescence intensity of the exciton line saturates in our InGaN quantum dot, and the fact that the low and high power pumping gives the same intensity in Fig. 3.3(b) after the addition of silver while being significantly different prior as shown in Fig. 3.3(a) demonstrates that we have enhanced the local field. This local field enhancement makes it easier to reach saturation with lower excitation power. To solidify our finding that the silver coating enhances the radiative rate sufficiently to overcome the metal losses as predicted by experiment we measure the before and after photoluminescence and time-resolved photoluminescence of many dots, with the results shown in Fig. 3.4. We find that before and after if no change is made to the sample, intensity and lifetime remain relatively constant as expected. If aluminum is added, which is not on plasmon resonance, the metal increases the nonradiative decay more than the radiative decay, resulting in a decrease in lifetime and intensity.

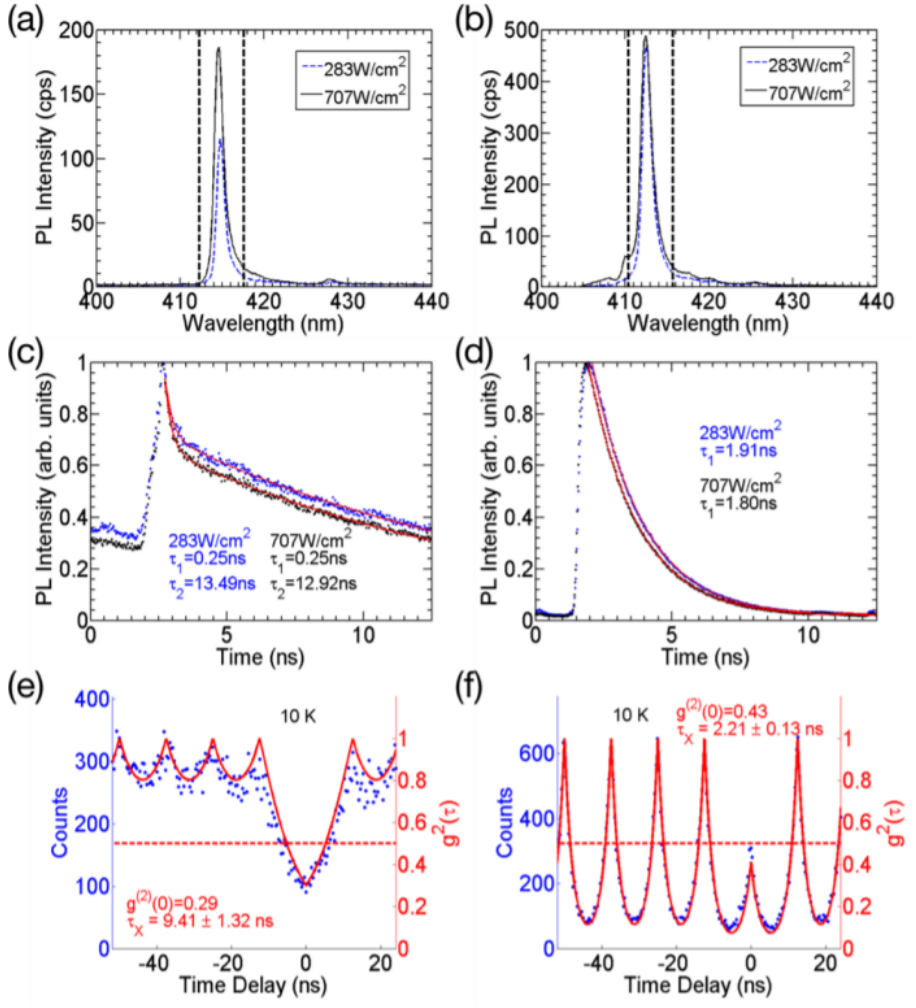

Figure 3.3: Taken from [18]. (a) photoluminescence before adding Ag (b) photoluminescence after adding Ag (c) time-resolved photoluminescence before adding Ag (d) time-resolved photoluminescence after adding Ag (e) $g^{(2)}$ before Ag (f) $g^{(2)}$ after Ag

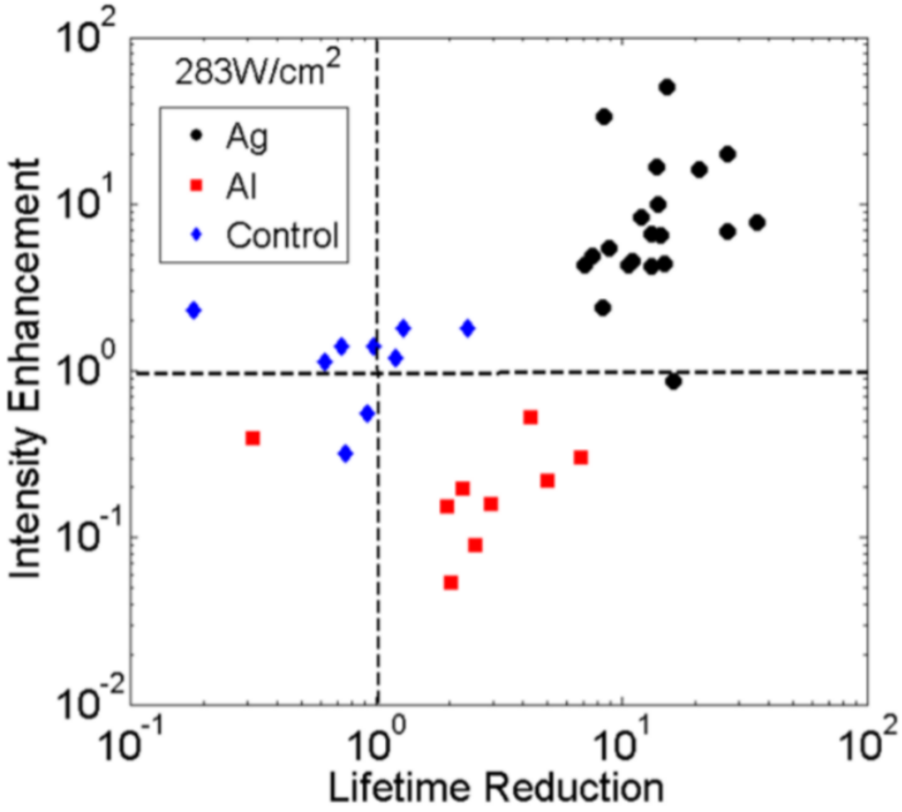

Figure 3.4: Taken from [18]. We show the intensity and lifetime enhancement across multiple quantum dots for no change (control, blue), addition of Aluminum (red), and addition of silver (black)

However, the addition of silver increases the intensity nearly an order of magnitude well reducing the lifetime an order and a half, indicating that the lifetime reduction is primarily radiative.

In conclusion, we demonstrated simultaneous broadband enhancement of the single photon emission of an array of InGaN quantum dots. This result is significant because it would be extremely difficult to replicate with photonic crystal cavities, and is an experimental demonstration the ability of plasmonic cavities to yield a net benefit to both emission rate and intensity despite losses in the metal.

CHAPTER IV

Cooperative light scattering in any dimensions

This chapter is a reproduction of the paper [35]. It presents a unified theory of cooperative light scattering valid for an open line, open plane, and open space.

4.1 Introduction

Interatomic dipole-dipole coupling yields remarkable collective effects such as super- and sub-radiant emission [20, 27, 19, 5], Anderson localization [74, 55], and collective Lamb shifts [49], which test fundamentals of quantum electrodynamics (QED) and have applications to superradiant lasers [7], quantum simulation [31], and protecting quantum information [52]. Waveguide quantum electrodynamics enables improved spatial mode matching compared to three-dimensional (3D) systems [56], thereby increasing photon-mediated coupling between distant atoms in one-dimensional (1D) [43, 32, 89, 47, 84, 73] and two-dimensional (2D) systems [55, 31]. We present an elegant unified model for cooperative light scattering by N two-level atoms in an open spatial region of arbitrary dimension d, providing a single expression for the collective effects in terms of "cardinal" Bessel functions. We propose a scheme to observe the phenomena in 2D using vacancy centers in diamond.

We develop a theory of multi-atom superradiance for electromagnetic fields confined to dD ($d \in [1, 2, 3]$). We solve the collective Lamb shifts and spontaneous emission rates as a function of dimension $d \in [1, 2, 3]$, dipole orientation, and dipole-dipole separation. We find that orientation effects are especially prominent at small atom-atom separations as dimension increases. Our theory provides intuition into how superradiance can be controlled via field confinement, orientation, and placement of dipoles in realistic structures such as our proposed diamond vacancy center scheme.

In our theory we find that 2D has the most complex orientation dependence between dipoles with subwavelength separations. This complex dependence is due to the lack of cylindrical symmetry with respect to the separation between dipoles, different from both 3D and 1D. Vacancy centers in diamond allow for subwavelength positioning of centers [83, 72, 73, 68] where the orientation-effects are especially prominent.

4.2 Quantum master equation in d dimensions

Our physical system comprises identical two-level systems (here called "atoms") coupled to electromagnetic fields propagating in vacuum. For a dD system, the fields are described by a plane-wave decomposition with wavevector $\boldsymbol{k} \in \mathbb{R}^d$ and dispersion $\omega_{\boldsymbol{k}} = c|\boldsymbol{k}|$. In this work a vector $\boldsymbol{a} = \sum_{l=1}^{3} x_l \hat{\boldsymbol{x}}_l \in \mathbb{R}^d$ if $\boldsymbol{a} \cdot \mathbb{1}_d = \boldsymbol{a} = \sum_{l=1}^{d} x_l \hat{\boldsymbol{x}}_l$, where $\mathbb{1}_d$ is the dD unit dyad $\sum_{l=1}^{d} \hat{\boldsymbol{x}}_l \hat{\boldsymbol{x}}_l$, which projects vectors into dD for $\{\hat{\boldsymbol{x}}_l\}$ the orthogonal Cartesian unit vectors.

We solve a master equation describing the evolution of atom states in our system, so following Lehmberg [49] we quantize the electromagnetic field. We consider the field quantized in a volume V, with photon creation operator $\hat{a}^{\dagger}_{\boldsymbol{k}l}$ producing a photon with wavevector $\boldsymbol{k}$, frequency $\omega_{\boldsymbol{k}}$, and polarization $\hat{\boldsymbol{e}}_l$, $\hat{\boldsymbol{k}} \cdot \hat{\boldsymbol{e}}_l = 0$. We can write the fields at point $\boldsymbol{r}$ as in (4.1),

$$\left\{ \begin{array}{c} \hat{\boldsymbol{E}}(\boldsymbol{r}) \\ \hat{\boldsymbol{B}}(\boldsymbol{r}) \end{array} \right\} = \sum_{k} \sum_{l=1}^{2} \sqrt{\frac{2\pi\omega_{\boldsymbol{k}}}{V}} \left\{ \begin{array}{c} \hat{\boldsymbol{e}}_l \\ \hat{\boldsymbol{k}} \times \hat{\boldsymbol{e}}_l \end{array} \right\} \left(e^{i\boldsymbol{k}\cdot\boldsymbol{r}} \hat{a}_{kl} + \mathrm{hc} \right) \tag{4.1}$$

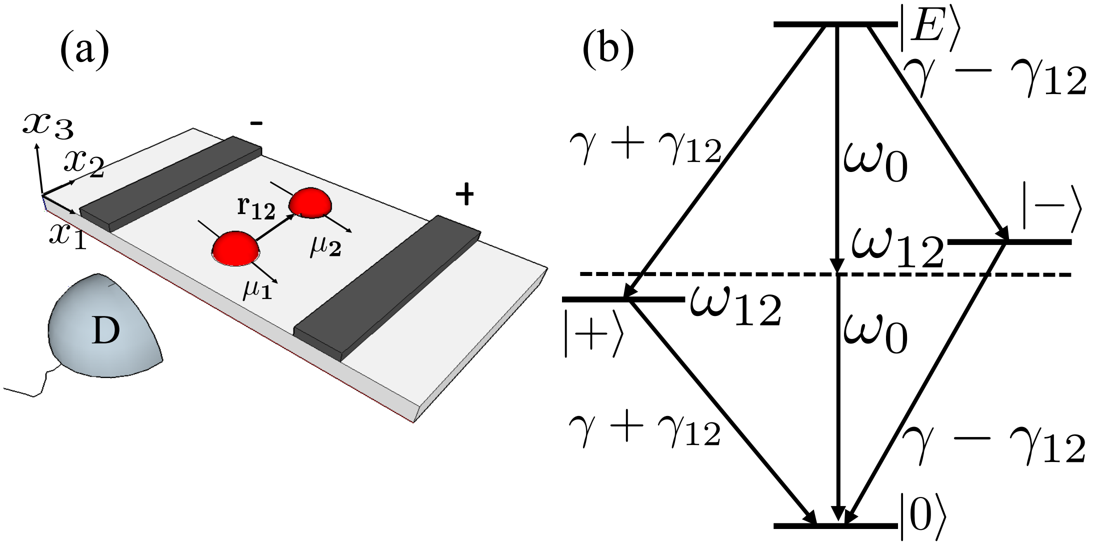

Figure 4.1: (a) Schematic showing a pair of emitters embedded in a 2D slab extending in the x_1x_2 plane. The emitters are separated a distance $\boldsymbol{r}_{\imath\jmath}$ apart in the $\hat{\boldsymbol{x}}_2$ direction. Emission is detected by a detector D. (b) Energy diagram for 2-atom superradiance, with $|0\rangle = |g\rangle_1|g\rangle_2$, $|E\rangle = |e\rangle_1|e\rangle_2$, and the superradiant and subradiant states $|\pm\rangle = \frac{1}{2}(|e\rangle_1|g\rangle_2 \pm |g\rangle_1|e\rangle_2)$. $|\pm\rangle$ have transition energies $\omega_0 \mp \omega_{12}$ and rates $\gamma \pm \gamma_{12}$, as labeled in diagram.

with hc denoting the hermitian conjugate and $\hat{}$ denoting operator or unit vector (which case pertains is discernible from the context).

Identical atoms are placed at positions $\boldsymbol{r} \in \mathbb{R}^d$. We label atoms with indices $\imath$ and $\jmath$ so that for atom $\imath$ energy $\hbar\omega_0$ separates its excited state $|\mathrm{e}\rangle_\imath$ from ground state $|\mathrm{g}\rangle_\imath$, and the atomic dipole moment $\boldsymbol{\mu}_\imath$ can be oriented in any direction in $\mathbb{R}^3$. Henceforth $\hbar \equiv 1$. De-exciting and exciting the atom is achieved by operators $\hat{\sigma}_\imath = |\mathrm{g}\rangle_\imath\langle\mathrm{e}|$ and $\hat{\sigma}_\imath^\dagger$, respectively.

Theorem IV.1. *The vacuum expectation of any self-adjoint N-atom operator $\hat{Q}$ for times $\omega_0 t \gg 1$ is*

$$\begin{aligned}\dot{\hat{Q}} =& \sum_{\imath\jmath}^{N} i\omega_{\imath\jmath}\left[\hat{\sigma}_\imath^\dagger\hat{\sigma}_\jmath, \hat{Q}\right] \\ &+ \frac{\gamma_{\imath\jmath}}{2}\left(2\hat{\sigma}_\imath^\dagger\hat{Q}\hat{\sigma}_\jmath - \hat{\sigma}_\imath^\dagger\hat{\sigma}_\jmath\hat{Q} - \hat{Q}\hat{\sigma}_\imath^\dagger\hat{\sigma}_\jmath\right)\end{aligned} \tag{4.2}$$

for $\omega_{\imath\imath} := \omega_0$*, and*

$$\begin{aligned}\omega_{\imath\jmath} =& -\frac{2\pi}{c^d}\int \text{đ}^{d-1}\Omega_{\hat{\boldsymbol{k}}}\boldsymbol{\mu}_\imath \cdot \left[\mathbb{1}_3 - \hat{\boldsymbol{k}}\hat{\boldsymbol{k}}\right]\cdot \boldsymbol{\mu}_\jmath \\ &\times \sum_{\pm}\mathcal{P}\int_0^\infty \text{đ}\omega \frac{\omega^d}{\omega \pm \omega_0} e^{i\omega\hat{\boldsymbol{k}}\cdot\boldsymbol{r}_{\imath\jmath}/c}, \qquad (4.3)\\ \gamma_{\imath\jmath} =& \frac{2\pi\omega_0^d}{c^d}\int \text{đ}^{d-1}\Omega_{\hat{\boldsymbol{k}}}\boldsymbol{\mu}_\imath \cdot \left[\mathbb{1}_3 - \hat{\boldsymbol{k}}\hat{\boldsymbol{k}}\right]\cdot \boldsymbol{\mu}_\jmath e^{i\omega_0\hat{\boldsymbol{k}}\cdot\boldsymbol{r}_{\imath\jmath}/c}, \qquad (4.4)\end{aligned}$$

with $\mathcal{P}$ *denoting principle value,* $\boldsymbol{r}_{\imath\jmath} := \boldsymbol{r}_\imath - \boldsymbol{r}_\jmath$, $\text{đ}^d := d^d/(2\pi)^d$, $d^{d-1}\Omega_{\hat{\boldsymbol{k}}}$ *the dD solid angle integrating over directions* $\hat{\boldsymbol{k}}$*.*

Proof. The Hamiltonian for N identical atoms (with individual frequency ω_0) coupled to the field is

$$\begin{aligned}\hat{H} =& \sum_{\imath=1}^N \omega_0\hat{\sigma}_\imath^\dagger\hat{\sigma}_\imath + \sum_{\boldsymbol{k}l}\omega_{\boldsymbol{k}}\hat{a}_{\boldsymbol{k}l}^\dagger\hat{a}_{\boldsymbol{k}l} - \sum_{\imath=1}^N\sum_{\boldsymbol{k}l}\left(\frac{2\pi\omega_{\boldsymbol{k}}}{V}\right)^{1/2} \\ &\times \hat{\boldsymbol{e}}_l \cdot \boldsymbol{\mu}_\imath \left(\mathrm{e}^{\mathrm{i}\boldsymbol{k}\cdot\boldsymbol{r}_\imath}\hat{a}_{\boldsymbol{k}l} + \mathrm{hc}\right)\left(\hat{\sigma}_\imath + \hat{\sigma}_\imath^\dagger\right). \qquad (4.5)\end{aligned}$$

The quantum master equation for $\hat{Q}$ any N-atom operator was originally solved for 3D fields by treating atoms as point dipoles and neglecting strong fields and non-local effects [49], and recently the master equation was solved for 1D fields [47]. Here we employ the Markovian approximation and solve for it in dD with $d \in [1, 2, 3]$ when the time of flight across the sample is faster than any spontaneous emission rate so that non-local effects may be neglected.

We first eliminate the photon operators $\hat{a}_{\boldsymbol{k}l}(0)$ which represents the field amplitude of the excitation source. We rewrite it in terms of atomic operators using

$$\begin{aligned}\hat{a}_{\boldsymbol{k}l}(t) =& \hat{a}_{\boldsymbol{k}l}(0)\mathrm{e}^{-\mathrm{i}\omega_{\boldsymbol{k}}t} + i\sum_\imath \left(\frac{2\pi\omega_{\boldsymbol{k}}}{V}\right)^{1/2}\hat{e}_l \cdot \boldsymbol{\mu}_\imath \mathrm{e}^{-\mathrm{i}\boldsymbol{k}\cdot\boldsymbol{r}_\imath} \\ &\times \int_0^t \mathrm{d}t'\left[\hat{\sigma}_\imath(t') + \hat{\sigma}_\imath^\dagger(t')\right]\mathrm{e}^{-\mathrm{i}\omega_{\boldsymbol{k}l}(t-t')}. \qquad (4.6)\end{aligned}$$

We then take vacuum expectation values of the master-equation solution to obtain

$$
\begin{aligned}
\dot{\hat{Q}} =& \mathrm{i}\omega_0 \sum_{\imath} \left[\hat{\sigma}_{\imath}^{\dagger}\hat{\sigma}_{\imath}, \hat{Q}\right] + \frac{1}{V}\sum_{\imath\jmath}\left[\sigma_{\imath} + \hat{\sigma}_{\imath}^{\dagger}, \hat{Q}\right] \\
& \times \left\{ \sum_{\boldsymbol{k}l} 2\pi\omega_{\boldsymbol{k}} (\hat{\boldsymbol{e}}_l \cdot \boldsymbol{\mu}_{\imath})\,(\hat{\boldsymbol{e}}_l \cdot \boldsymbol{\mu}_{\jmath})\, \mathrm{e}^{\mathrm{i}\boldsymbol{k}\cdot\boldsymbol{r}_{\imath\jmath}} \right. \\
& \left. \times \left[f_-\hat{\sigma}_{\jmath} + f_+\hat{\sigma}_{\jmath}^{\dagger}\right] + \mathrm{hc} \right\}
\end{aligned}
\tag{4.7}
$$

with $f_{\pm} = -i\mathcal{P}(\omega \pm \omega_0)^{-1} + \pi\delta(\omega \pm \omega_0)$.

We then express the master equation in terms of collective frequency shifts and corresponding linewidths, which involves converting the sum over $\boldsymbol{k}$ into integration over $\omega(\boldsymbol{k})$ using the dispersion relation $\omega = \mathrm{c}\,|\boldsymbol{k}|$ and obtain

$$
\frac{1}{V}\sum_{\boldsymbol{k}} \to \int \text{đ}^d\boldsymbol{k} \to \frac{1}{\mathrm{c}^d}\int \text{đ}\omega\,\omega^{d-1}\int \text{đ}^{d-1}\Omega_{\hat{\boldsymbol{k}}}, \tag{4.8}
$$

$$
\mathrm{d}^{d-1}\Omega_{\hat{\boldsymbol{k}}} = \prod_{l=1}^{d-1} \sin^{d-l-1}\theta_l \mathrm{d}\theta_l. \tag{4.9}
$$

Here $\mathrm{d}^{d-1}\Omega_{\hat{\boldsymbol{k}}}$ is the dD solid angle over directions $\hat{\boldsymbol{k}}$ with azimuthal angles $\theta_1, \ldots, \theta_{d-2} \in [0,\pi]$ and polar angle $\theta_{d-1} \in [0, 2\pi)$. Substituting

$$
\sum_{l=1}^{2} (\hat{\boldsymbol{e}}_l \cdot \boldsymbol{\mu}_{\imath})\,(\hat{\boldsymbol{e}}_l \cdot \boldsymbol{\mu}_{\jmath}) = \boldsymbol{\mu}_{\imath} \cdot (\mathbb{1}_3 - \hat{\boldsymbol{k}}\hat{\boldsymbol{k}}) \cdot \boldsymbol{\mu}_{\jmath}, \tag{4.10}
$$

and Eq. (4.8) into Eq. (4.7) completes the proof. $\square$

For $N = 1$ atom and a dD field, with $k_0 := \omega_0/\mathrm{c} = 2\pi/\lambda_0$ and $\boldsymbol{\mu}_{\imath} := \mu_{\imath}\hat{\boldsymbol{\mu}}_{\imath}$, Eq. (4.4) yields spontaneous emission rate

$$
\gamma_{\imath\imath} = \frac{2^{3-d}\pi^{2-d/2}\mu_{\imath}^2 k_0^d}{\Gamma(d/2)}\left(1 - \frac{\hat{\boldsymbol{\mu}}_{\imath} \cdot \mathbb{1}_d \cdot \hat{\boldsymbol{\mu}}_{\imath}}{d}\right) \tag{4.11}
$$

for Γ the Gamma function. In 3D, $\gamma_{\imath\imath} = 4\mu_{\imath}^2 k_0^3/3$ is independent of dipole orientation.

In 1D and 2D, $\gamma_{\imath\imath}$ is maximized for the dipole perpendicular to the $\mathbb{R}^d$ subspace ($\hat{\boldsymbol{\mu}}_\imath \cdot \mathbb{1}_d \cdot \hat{\boldsymbol{\mu}}_\imath = 0$) and thus falls by half for in-plane dipoles in 2D ($\hat{\boldsymbol{\mu}}_\imath \cdot \mathbb{1}_2 \cdot \hat{\boldsymbol{\mu}}_\imath = 1$) compared to out-of-plane dipoles [55] and is zero for in-line dipoles in 1D.

For $r_{\imath\jmath} \ll \lambda$, Eq. (4.3) is divergent and cannot be used to calculate the single-atom Lamb shift. The breakdown of this theory to describe the single-atom Lamb shift is a consequence of approximating a physical dipole with a point dipole. We thus treat the single-atom Lamb shift as being incorporated into a renormalized frequency ω_0.

For $N \geq 2$ atoms, signatures of collective-effects, such as enhanced spontaneous decay and Lamb shifts, are quantified by $\gamma_{\imath\jmath}$ and $\omega_{\imath\jmath}$ ($\imath \neq \jmath$), respectively, as illustrated in Fig. 4.1(b) for $N = 2$ atoms. We now express $\gamma_{\imath\jmath}$ and $\omega_{\imath\jmath}$ in terms of the dD dyadic Green's function.

Definition IV.2. The dyadic Green's function in dD is $\overleftrightarrow{G}_d := \mathcal{D} G_d$ for $\mathcal{D} := \mathbb{1}_3 + \frac{1}{k_0^2} \nabla_d \nabla_d$ a dyadic operator, G_d the solution of the dD Helmholtz equation $\left[\nabla_d^2 + k_0^2\right] G_d\left(\boldsymbol{r}_{\imath\jmath}, \omega_0\right) = -\delta\left(\boldsymbol{r}_{\imath\jmath}\right)$.

Definition IV.3. Analogous to the relation between $\sin x$ and $\operatorname{sinc} x$ ("cardinal sine"), we introduce "cardinal" versions of the Bessel functions (first and second kind) and Hankel function of the first kind as, respectively,

$$\check{J}_\alpha(x) := \frac{J_\alpha(x)}{x^\alpha},\ \check{Y}_\alpha(x) := \frac{Y_\alpha(x)}{x^\alpha},\ \check{H}_\alpha^{(1)}(x) := \frac{H_\alpha^{(1)}(x)}{x^\alpha}.$$

Theorem IV.4. *The complex collective frequency shift is*

$$\Gamma_{\imath\jmath} := -\omega_{\imath\jmath} + i\gamma_{\imath\jmath}/2 = 4\pi k_0^2 \boldsymbol{\mu}_\imath \cdot \overleftrightarrow{G}_d(\boldsymbol{r}_{\imath\jmath}, \omega_0) \cdot \boldsymbol{\mu}_\jmath. \tag{4.12}$$

Proof. Solutions of the dD Helmholtz equation are [75] $A\check{J}_{d/2-1}\left(\tilde{r}_{\imath\jmath}\right) + B\check{Y}_{d/2-1}\left(\tilde{r}_{\imath\jmath}\right)$ for $\tilde{\boldsymbol{r}}_{\imath\jmath} := k_0 \boldsymbol{r}_{\imath\jmath} = \tilde{r}_{\imath\jmath} \hat{\tilde{\boldsymbol{r}}}_{\imath\jmath}$ and A and B arbitrary complex constants. Imposing the

Sommerfeld radiation condition

$$\lim_{\tilde{r}_{\imath\jmath}\to\infty} |\boldsymbol{r}_{\imath\jmath}|^{(d-1)/2} \left(\frac{\partial}{\partial \tilde{r}_{\imath\jmath}} - \mathrm{i}\right) G_d\left(\boldsymbol{r}_{\imath\jmath}, \omega_0\right) = 0. \tag{4.13}$$

on an outgoing spherical wave satisfying energy conservation yields the purely radial expression

$$G_d\left(\boldsymbol{r}_{\imath\jmath}, \omega_0\right) = \frac{\mathrm{i}}{4}\left[\frac{k_0^2}{2\pi}\right]^{d/2-1} \check{H}^{(1)}_{d/2-1}\left(\tilde{r}_{\imath\jmath}\right). \tag{4.14}$$

For $G_d' := \frac{\mathrm{d}G_d}{\mathrm{d}\tilde{r}_{\imath\jmath}}$ and $G_d'' := \frac{\mathrm{d}^2 G_d}{\mathrm{d}\tilde{r}^2_{\imath\jmath}}$, applying $\mathcal{D}$ to G_d (4.14) yields

$$\frac{1}{k_0^2}\nabla_d\nabla_d G_d = \hat{\boldsymbol{r}}_{\imath\jmath}\hat{\boldsymbol{r}}_{\imath\jmath} G_d'' + \frac{\nabla_d \hat{\boldsymbol{r}}_{\imath\jmath}}{k_0} G_d'. \tag{4.15}$$

We apply the identity

$$\frac{\nabla_d \hat{\boldsymbol{r}}_{\imath\jmath}}{k_0} = \frac{1}{\tilde{r}_{\imath\jmath}}(\mathbb{1}_d - \hat{\boldsymbol{r}}_{\imath\jmath}\hat{\boldsymbol{r}}_{\imath\jmath}) \tag{4.16}$$

to obtain

$$\frac{1}{k_0^2}\nabla_d\nabla_d G_d = \frac{1}{\tilde{r}_{\imath\jmath}} G_d' \mathbb{1}_d + \left(G_d'' - \frac{1}{\tilde{r}_{\imath\jmath}} G_d'\right)\hat{\boldsymbol{r}}_{\imath\jmath}\hat{\boldsymbol{r}}_{\imath\jmath}. \tag{4.17}$$

Hankel function recurrence relations then yield

$$\begin{aligned}\overleftrightarrow{G}_d\left(\tilde{\boldsymbol{r}}_{\imath\jmath}, \omega_0\right) =& \frac{\mathrm{i}}{4}\left[\frac{k_0^2}{2\pi}\right]^{d/2-1}\Bigg(\check{H}^{(1)}_{d/2-1}\left(\tilde{r}_{\imath\jmath}\right)\left[\mathbb{1}_3 - \hat{\boldsymbol{r}}_{\imath\jmath}\hat{\boldsymbol{r}}_{\imath\jmath}\right] \\ & - \check{H}^{(1)}_{d/2}\left(\tilde{r}_{\imath\jmath}\right)\left[\mathbb{1}_d - d\hat{\boldsymbol{r}}_{\imath\jmath}\hat{\boldsymbol{r}}_{\imath\jmath}\right]\Bigg).\end{aligned} \tag{4.18}$$

We now obtain $\Gamma_{\imath\jmath}$ directly from Eqs. (4.3) and (4.4). Substituting

$$-k_0^2 \hat{\boldsymbol{k}}\hat{\boldsymbol{k}} \mathrm{e}^{\mathrm{i}\omega\hat{\boldsymbol{k}}\cdot\boldsymbol{r}_{\imath\jmath}/c} = \nabla_d\nabla_d \mathrm{e}^{\mathrm{i}\hat{\boldsymbol{k}}\cdot\boldsymbol{r}_{\imath\jmath}\omega_0/c},\ \boldsymbol{r}_{\imath\jmath} \neq \boldsymbol{0}, \tag{4.19}$$

into Eq. (4.4), and using

$$\int \mathrm{d}^{d-1}\Omega_{\hat{\boldsymbol{k}}} \mathrm{e}^{\mathrm{i}\hat{\boldsymbol{k}}\cdot\boldsymbol{r}_{\imath\jmath}\omega_0/c} = (2\pi)^{d/2}\,\check{J}_{d/2-1}\left(\tilde{r}_{\imath\jmath}\right), \tag{4.20}$$

yields

$$\gamma_{\imath\jmath} = \frac{k_0^d}{(2\pi)^{d-2}} \boldsymbol{\mu}_\imath \cdot \mathcal{D}\left[(2\pi)^{d/2} \check{J}_{d/2-1}\left(\tilde{r}_{\imath\jmath}\right)\right] \cdot \boldsymbol{\mu}_\jmath. \tag{4.21}$$

Similarly,

$$\omega_{\imath\jmath} = \frac{1}{2} \frac{k_0^d}{(2\pi)^{d-2}} \boldsymbol{\mu}_\imath \cdot \mathcal{D}\left[(2\pi)^{d/2} \check{Y}_{d/2-1}\left(\tilde{r}_{\imath\jmath}\right)\right] \cdot \boldsymbol{\mu}_\jmath. \tag{4.22}$$

Comparing Eqs. (4.21) and (4.22) with (4.18) proves the result. □

4.3 Analysis of collective effects

Equation (4.12) is a unified solution of collective atom-atom couplings for dD, and includes the previous results for 1D [47], 2D [55], and 3D [49]. Now we separate the terms governing the separation and orientation dependence of the collective atom-atom coupling by rewriting Eq. (4.12) as

$$\Gamma_{\imath\jmath} = \frac{\mathrm{i}}{2} \frac{\mu_\imath \mu_\jmath k_0^d}{(2\pi)^{d/2-2}} \left(\check{H}^{(1)}_{d/2-1}\left(\tilde{r}_{\imath\jmath}\right) \Theta_{\imath\jmath} - \check{H}^{(1)}_{d/2}\left(\tilde{r}_{\imath\jmath}\right) \Theta'_{\imath\jmath}\right) \tag{4.23}$$

for

$$\begin{aligned} \Theta_{\imath\jmath} =& \hat{\boldsymbol{\mu}}_\imath \cdot \hat{\boldsymbol{\mu}}_\jmath - (\hat{\boldsymbol{\mu}}_\imath \cdot \hat{\boldsymbol{r}}_{\imath\jmath})(\hat{\boldsymbol{\mu}}_\jmath \cdot \hat{\boldsymbol{r}}_{\imath\jmath}), && (4.24) \\ \Theta'_{\imath\jmath} =& \hat{\boldsymbol{\mu}}_\imath \cdot \mathbb{1}_d \cdot \hat{\boldsymbol{\mu}}_\jmath - d(\hat{\boldsymbol{\mu}}_\imath \cdot \hat{\boldsymbol{r}}_{\imath\jmath})(\hat{\boldsymbol{\mu}}_\jmath \cdot \hat{\boldsymbol{r}}_{\imath\jmath}). && (4.25) \end{aligned}$$

Here the cardinal Hankel functions express the separation dependence of the collective effects, whereas (4.24) and (4.25) summarize the orientation dependence of these effects. Asymptotically $\tilde{r}_{\imath\jmath} \gg 1$,

$$\check{H}^{(1)}_{d/2-1}\left(\tilde{r}_{\imath\jmath}\right) \to \frac{\exp\left\{\mathrm{i}\left[\tilde{r}_{\imath\jmath} - \frac{\pi}{4}(d-1)\right]\right\}}{\tilde{r}_{\imath\jmath}^{\frac{d-1}{2}}}, \tag{4.26}$$

leading to $\check{H}^{(1)}_{d/2-1}\left(\tilde{r}_{\imath\jmath}\right)/\check{H}^{(1)}_{d/2}\left(\tilde{r}_{\imath\jmath}\right) \to \mathrm{i}\tilde{r}_{\imath\jmath}$, which shows that the first term in Eq. (4.23) dominates for $\tilde{r}_{\imath\jmath} \gg 1$ (defined here as far field) and the second term in Eq. (4.23) which typically dominates for near field, defined as $\tilde{r}_{\imath\jmath} \ll 1$. We see that the near- and far-field terms are $\pi/2$ out of phase, so it is possible to use orientation control to suppress either $\gamma_{\imath\jmath}$ or $\omega_{\imath\jmath}$ by a factor of $\tilde{r}_{\imath\jmath}$ for distant atoms.

Now we examine angular dependence of $\Gamma_{\imath\jmath}$ (4.23) by studying the properties of $\Theta_{\imath\jmath}$ (4.24) and $\Theta'_{\imath\jmath}$ (4.25). We restrict to parallel dipoles ($\hat{\boldsymbol{\mu}}_\imath = \hat{\boldsymbol{\mu}}_\jmath$) separated along the x_1 axis ($\hat{\boldsymbol{r}}_{\imath\jmath} = \hat{\boldsymbol{x}}_1$) to visualize the angular dependence. In the far-field, the angular dependence is governed by the d-independent term $\Theta_{\imath\jmath} = 1 - \left(\hat{\boldsymbol{\mu}}_\imath \cdot \hat{\boldsymbol{x}}_1\right)^2$. Setting $\hat{\boldsymbol{\mu}}_\imath = \sin\theta_1\cos\theta_2\hat{\boldsymbol{x}}_1 + \sin\theta_1\sin\theta_2\hat{\boldsymbol{x}}_2 + \cos\theta_1\hat{\boldsymbol{x}}_3$ yields $\Theta_{\imath\jmath} = 1 - \sin^2\theta_1\cos^2\theta_2$, which is a torus. In the near field, Γ becomes d-dependent with

$$\Theta'_{\imath\jmath} = \begin{cases} 0, & d = 1, \\ -\sin^2\theta_1\cos 2\theta_2, & d = 2, \\ 1 - 3\sin^2\theta_1\cos^2\theta_2, & d = 3. \end{cases} \tag{4.27}$$

We plot real and imaginary parts of $\Gamma_{\imath\jmath}$ in Fig. 4.2 for parallel dipoles as functions of dipole orientation $\hat{\boldsymbol{\mu}}_\imath$ given by x_1,x_2,x_3. The interatomic separation is fixed to be very small ($\tilde{r}_{\imath\jmath} \ll 1$) in order to correspond to the Dicke limit. The cylindrical symmetry of $\omega_{\imath\jmath}$ for the 1D and 3D cases, as seen in Fig. 4.2(a,c), is replaced the four-leaf structure in 2D shown in Fig. 4.2(b), and the simple plot of $\gamma_{\imath\jmath}$ in Fig. 4.2(f) transforms to more complicated surfaces in Fig. 4.2(d,e) due to enhanced emission for atoms oriented perpendicular to its confinement.

Collective effects (4.23) are strongly dependent on dimensional confinement, as evidenced by the contrast between inverse-distance dependence in 3D vs constant in 1D for large separation $\tilde{r}_{\imath\jmath} \gg 1$ [49, 47]. The d-dependence of $\Gamma_{\imath\jmath}$ is captured by the asymptotic expression for the cardinal Hankel function (4.26) whose denominator

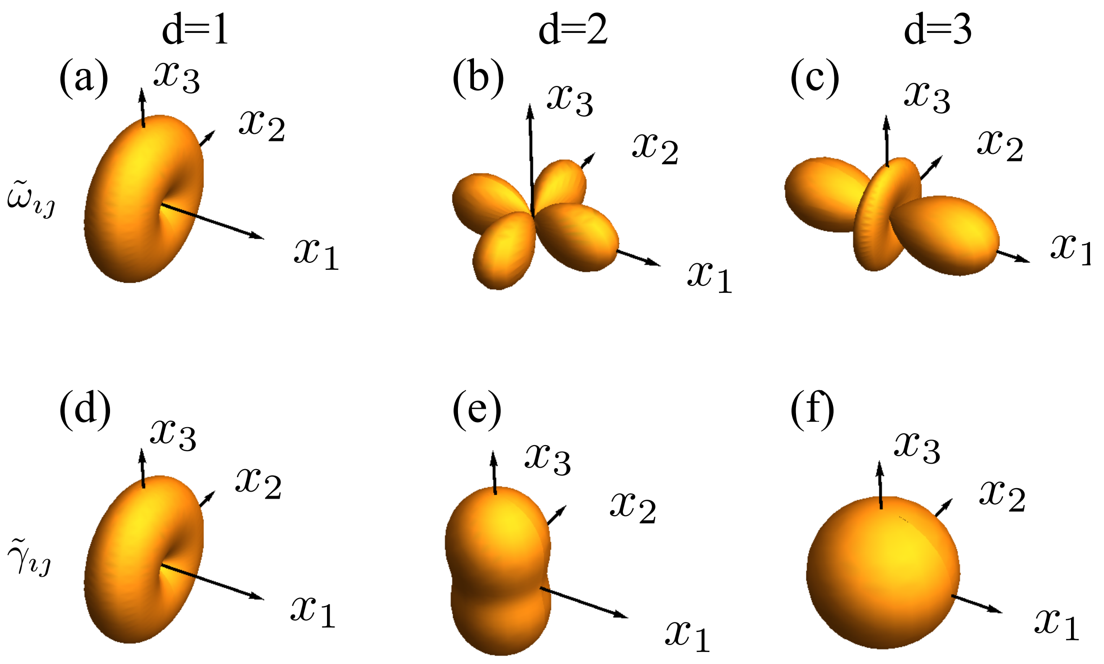

Figure 4.2: Spherical polar plots of dimensionless $\tilde{\omega}_{12} = \omega_{12}/\gamma_{11}$ (a)-(c) and $\tilde{\gamma}_{12} = \gamma_{12}/\gamma_{11}$ (d)-(f) up to a multiplicative constant for parallel dipoles $\boldsymbol{\mu}_1 = \boldsymbol{\mu}_2 = \sum_{l=1}^{3} x_l \hat{\boldsymbol{x}}_l$, $r_{12} \ll \lambda$, and $\hat{\boldsymbol{r}}_{12} = \hat{\boldsymbol{x}}_1$.

shows d-dependent fall-off and whose oscillatory exponential numerator shows that $\gamma_{\imath\jmath}$ and $\omega_{\imath\jmath}$ are $\pi/2$ out of phase. Furthermore $\check{H}^{(1)}_{d/2-1}$ experiences a $\pi/4$ phase shift for each integer leap in dimension d, corresponding to a $\lambda_0/8$ shift in relative positions of the atoms in different dimensions for maximizing atom-field coupling.

Whereas $\omega_{\imath\jmath}$ and $\gamma_{\imath\jmath}$ display similar features for well separated parallel dipoles, the closely spaced parallel-dipole case is quite different due to $\gamma_{\imath\jmath}$ being sensitive to both near- and far-field terms in (4.23) while $\omega_{\imath\jmath}$ is only sensitive to near field terms. Specifically, the asymptotic expressions for the cardinal Bessel functions yield

$\gamma_{\imath\jmath} \mapsto \gamma_{\imath\imath}\left[1-\mathcal{O}(\tilde{r}_{\imath\jmath}^2)\right]$, which is independent of d, whereas

$$\omega_{\imath\jmath} \sim \begin{cases} \tilde{r}_{\imath\jmath}^{-d}, & \Theta'_{\imath\jmath} \neq 0, \\ \tilde{r}_{\imath\jmath}^{-d+2}, & \Theta'_{\imath\jmath} = 0, d \neq 2, \\ \log \tilde{r}_{\imath\jmath}, & \Theta'_{\imath\jmath} = 0, d = 2. \end{cases} \tag{4.28}$$

We now have asymptotic expressions of $\gamma_{\imath\jmath}$ and $\omega_{\imath\jmath}$ in the asymptotic small and large $\tilde{r}_{\imath\jmath}$ regimes and now explore the dependence on the full range of $\tilde{r}_{\imath\jmath}$.

We plot each of $\omega_{\imath\jmath}$ and $\gamma_{\imath\jmath}$ as a function of both $\tilde{r}_{\imath\jmath}$ and d as surface plots in Fig. 4.3(a,c) and present slices of those plots in Fig. 4.3(b,d). We have interpolated between integer dimensions by inserting the modified identity

$$\mathbb{1}_d = \sum_{l=1}^{\lceil d \rceil} \hat{\boldsymbol{x}}_l \hat{\boldsymbol{x}}_l + (d - \lceil d \rceil)\, \hat{\boldsymbol{x}}_{\lceil d \rceil} \hat{\boldsymbol{x}}_{\lceil d \rceil} \tag{4.29}$$

into Eq. (4.25), where $\lceil\ \rceil$ is the ceiling function. The small and large $\tilde{r}_{\imath\jmath}$ features have been explained already, and the plot shows that these small and large limits apply everywhere except a small region near $\tilde{r}_{\imath\jmath} \sim 1$. Interestingly our d-dependent functions are smooth for real-valued d, thus giving us clear predictions of collective behavior for non-integer dimension. Exploration of non-integer d collective effects would be quite interesting and could relate to electromagnetic field anisotropy [33].

4.4 Experimental proposal for observation of collective effects in two dimensions

As 1D and 3D collective effects have been explored experimentally, we propose a 2D experiment with vacancy centers in diamond as our “atoms”. In addition to requiring a structure that confines the electromagnetic field to 2D, we have three requirements for the emitters for realizing 2D superradiance: sub-wavelength relative

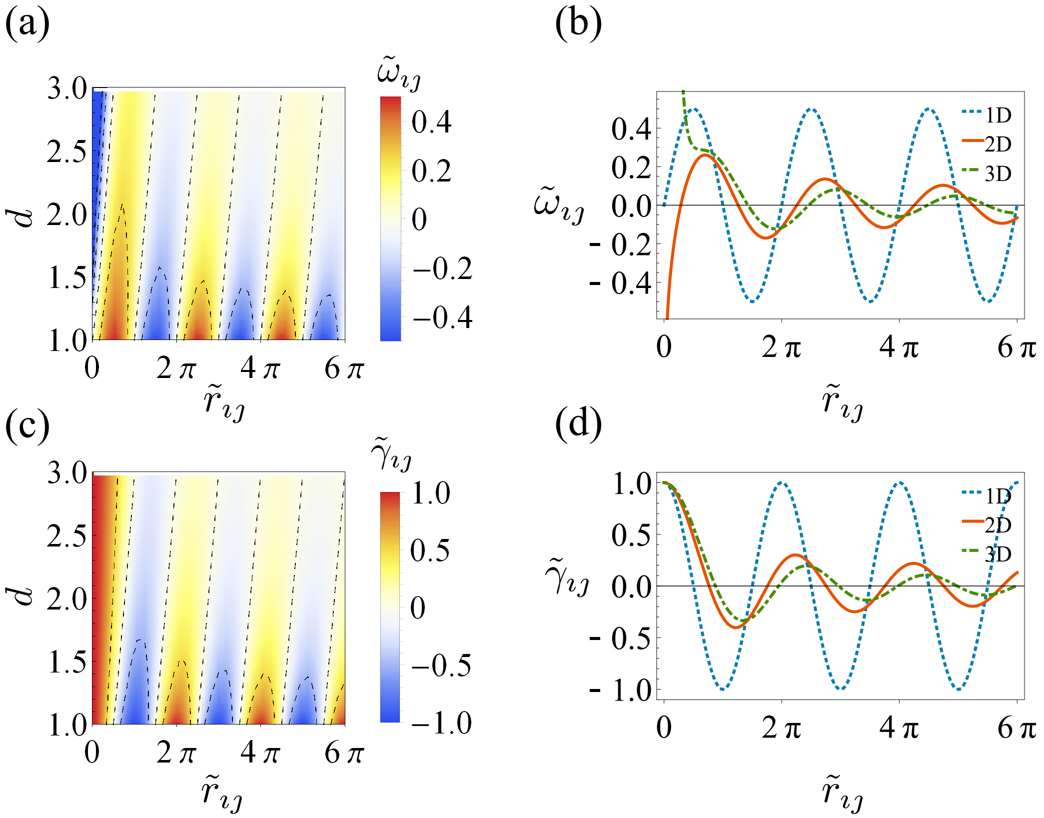

Figure 4.3: (Color online) Dimensional and separation dependence of dimensionless $\tilde{\omega}_{\imath\jmath} := \omega_{\imath\jmath}/\gamma_{\imath\imath}$ ((a)-(b)) and $\tilde{\gamma}_{\imath\jmath} := \gamma_{\imath\jmath}/\gamma_{\imath\imath}$ ((c)-(d)) vs dimensionless separation $\tilde{r}_{\imath\jmath} = 2\pi\frac{r_{\imath\jmath}}{\lambda}$ for identical parallel dipoles $\hat{\boldsymbol{\mu}}_\imath = \hat{\boldsymbol{\mu}}_\jmath = \hat{\boldsymbol{x}}_3$. (a) and (c) show results interpolated for real valued dimensions $1 \leq d \leq 3$. (b) and (d) compare $d = 1$ (dotted blue line), $d = 2$ (solid red line), $d = 3$ (dot-dashed green line).

position control, lifetime-limited linewidths, and spectrally overlapping energies. The 2D structure and emitter-position control ensure the ability to control superradiance phenomena, while the spectral requirements are necessary for their observation.

There are two promising approaches towards a 2D diamond structure: ultra-high aspect ratio diamond thinned via plasma etching [82] and membrane structures of sub-wavelength thicknesses [62]. As the diamond medium is not the vacuum described thus far, we extend our result to dielectric media using [45, 4]

$$\Gamma_{\imath\jmath,\epsilon(\omega)}(r_{\imath\jmath}) = \mathrm{Re}\left[\epsilon(\omega_0)^{1/2}\right] |l|^2 \Gamma_{\imath\jmath}\left(\mathrm{Re}\left[\epsilon(\omega_0)^{1/2}\right] r_{\imath\jmath}\right), \tag{4.30}$$

where $\epsilon(\omega)$ is the dielectric coefficient, and l is a local electric field factor.

To satisfy the requirements on the emitters, ion implantation techniques allow either nitrogen or silicon vacancies to be positioned with impressive $r_{\imath\jmath} \sim \lambda_0/20$ accuracy [83, 72, 73, 68]. We propose working with a single pair of vacancies as shown in Fig. 4.1(a) to minimize inhomogeneity inherent in an ensemble. Nitrogen vacancy centers are appealing due to their narrow homogeneous linewidths [70] but suffer from strain-induced inhomogeneous broadening that can be ameliorated by Stark shifting from an external field [80].In contrast, silicon vacancies have inversion symmetry that protects them from external fields, thereby reducing inhomogeneity but makes spectral control via Stark shifts challenging [68]. However each silicon vacancy can be addressed with a tunable off-resonant laser to obtain spectrally overlapping Raman transitions, as has been used to demonstrate 1D superradiance [73].

For either nitrogen- or silicon- vacancy centers, the pair can be excited symmetrically by a resonant pulse with bandwidth much less than $\gamma_{\imath\imath}$ and propagating perpendicular to $\boldsymbol{r}_{\imath\jmath}$. Superradiant effects can be quantified by $\omega_{\imath\jmath}(\tilde{r}_{\imath\jmath}, \boldsymbol{\mu}_\imath, \boldsymbol{\mu}_\jmath)$ and $\gamma_{\imath\jmath}(\tilde{r}_{\imath\jmath}, \boldsymbol{\mu}_\imath, \boldsymbol{\mu}_\jmath)$ through time-resolved photoluminescence measurements as outlined in Fig. 4.1(b).

4.5 Conclusions

In conclusion, we present a unified solution for collective spontaneous emission, for electromagnetic field confined to dimension $d \in [1, 2, 3]$, with arbitrary dipole orientation and separation. We explain the scaling behavior of cooperative effects for systems much larger or smaller than the resonance wavelength. Furthermore we suggest a potential implementation scheme using vacancy centers in diamond to explore the effects in 2D.

CHAPTER V

Super- and sub-radiance

5.1 Introduction

In this section we apply the theory of cooperative light scattering to multi-atom systems to show the emergence of collective modes of the system with very rapid decay rates. In 1954 Dicke [20] showed that N identical atoms each with single atom decay rate Γ_0 in their excited state in a subwavelength volume form a collective mode that decays at $\Gamma = N\Gamma_0$. Because their are N atoms, at short times the total emission rate is proportional to N^2. Later work studied the effect when the atoms spacing grew beyond the subwavelength limit [49, 57].

5.1.1 Single photon superradiance

For the case of a single photon excitation, the analytic theory underlying superradiance simplifies considerably. To see why, we consider that for N two-level emitters, there are 2^N possible states, where each factor of 2 is whether a given atom is excited or not excited. In this case of very low excitation power such that only one atom can be excited, we instead only have N possible excited states. Thus, when considering many atoms, it quickly becomes vastly simpler analytically to consider the low power limit. In particular, these N coupled states lead to N collective modes, where the modes that that emit more rapidly than the single-atom case are called superradiance modes and those that emit more slowly are called sub-radiant modes. The coupling between the N atoms can be considered pairwise, in which case we can construct an $N \times N$ matrix that describes the coupling. Since their are N total 1-atom excited states, we expect that once coupling is included, we can still describe the system by N different eigenstates of $N \times N$ coupling matrix. In this way, single photon superradiance may be described as a many-body eigenvalue problem [76, 78, 79]. In our work, we will consider this approach.

5.1.1.1 Atomic clouds

Studies have been done on superradiance in extended atomic cloud samples in three dimensions. To effectively treat the many-atom case, it is common to consider the case of single-photon excitation [76]. For extended samples, evolution depends on an effective Rabi frequency $\Omega \propto \sqrt{N}$. If the time of flight is greater than this characteristic time $\Omega R/c \gg 1$, then there are oscillations between a collective state and a ground state with frequenct Ω and rate c/R. However, if the time of flight across the sample is short, $\Omega R/c < 1$, then the state exponentially decays with rate proportional to N as in the Dicke limit.

For the case where the sample is excited by as single atom, it is frequently assumed the initial state is the timed Dicke state [76]

$$|+\rangle_{\boldsymbol{k}_0} = \frac{1}{\sqrt{N}} \sum_{j=1}^{N} e^{i\boldsymbol{k}_0 \cdot \boldsymbol{r}_j} |g_1, g_2, \ldots e_j, \ldots, g_N\rangle \tag{5.1}$$

where $|g_1, g_2, \ldots e_j, \ldots, g_N\rangle$ is a fox state with only atom j excited and the others in the ground state.

Beyond simply increased emission, there are further signatures of superradiance. It is found that the radiation is directional coincident with the direction of excitation [49, 76, 15]. Futhermore, the radiation pressure and absorption are both affected by the superradiance phenomena [15]

5.1.1.2 Superradiance and cooperative effects on atom lattices

In addition to a uniform cloud, another critical geometry to consider collective effects is on a regularly spaced lattice of atoms. Because atoms can interact as a phased array, the exact spacing can be critical to determine the overall emission. For atoms trapped optically in a lattice with spacing d_0 and length L and wavelength λ, the collective emission rate is found to be [63]

$$\Gamma_{1D} \propto \lambda/d_0 \tag{5.2}$$

$$\Gamma_{3D} \propto (\lambda/d_0)^2(L/d_0) \tag{5.3}$$

5.1.1.3 Virtual Lamb shifts

If we consider N two level atoms with evergy levels a and b, with $E_a - E_b = \hbar\omega$, which are prepared in a one atom excited state (such as the timed Dicke state). If $\beta(t, \boldsymbol{r})$ is the probability amplitude of excitation, i.e. the probabilty to find an atom at position $\boldsymbol{r}$ excited at time t. If we assume a dense cloud on a volume V such that their are $\gg 1$ atom per volume λ^3, then the amplitude evolves as

$$\frac{\partial\beta(t,\boldsymbol{r})}{\partial t} = i\gamma\frac{N}{V}\int \mathrm{d}\boldsymbol{r}'\frac{\exp(ik_0|\boldsymbol{r}-\boldsymbol{r}'|)}{k_0|\boldsymbol{r}-\boldsymbol{r}'|}\beta(t,\boldsymbol{r}') \tag{5.4}$$

Here γ is the single atom decay rate. The integration kernel can be separated in terms of the real and virtual transitions as [28, 78, 29, 79, 77]

$$\frac{\partial\beta(t,\boldsymbol{r})}{\partial t} = i\gamma\frac{N}{V}\int \mathrm{d}\boldsymbol{r}'\left[\frac{\cos(ik_0|\boldsymbol{r}-\boldsymbol{r}'|)}{k_0|\boldsymbol{r}-\boldsymbol{r}'|} + i\frac{\sin(ik_0|\boldsymbol{r}-\boldsymbol{r}'|)}{k_0|\boldsymbol{r}-\boldsymbol{r}'|}\right]\beta(t,\boldsymbol{r}') \tag{5.5}$$

Here the sine term corresponds to the real transitions [23], while the cosine term corresponds to virtual transitions [79, 77]. These virtual transitions play an important role in the overall superradiance effects of the system, and in particular can lead to population trapping in the subradiant state [79].

5.1.1.4 Non-local effects

If we assume a dense cloud as in the previous section, that is large compared to the time of flight, then we must include relativistic retardation effects to accurately describe the system. If we include time of flight, then

$$\frac{\partial\beta(t,\boldsymbol{r})}{\partial t} = i\gamma\frac{N}{V}\int \mathrm{d}\boldsymbol{r}'\frac{\exp(ik_0|\boldsymbol{r}-\boldsymbol{r}'|)}{k_0|\boldsymbol{r}-\boldsymbol{r}'|}\beta(t-\frac{|\boldsymbol{r}-\boldsymbol{r}'|}{c},\boldsymbol{r}') \tag{5.6}$$

5.1.1.5 Directional Emission

The collective mode of a many-atom system can be highly directional [49, 76, 15, 58]. In particular, it has been found that several hundred atoms can interact with a single mode of light to provide highly directional single photon emission [58], where the spatial emission profile can be controlled by manipulating the geometry of the atomic array. The authors note they also obtain temporal control over the emitted wave-packet, which suggests that collective mode emission may be a promising single photon source candidate for applications in quantum communication networks.

5.1.2 Few atom superradiance

While an analytic solution in the N-atom case exponentially difficult for large N, one can obtain solutions in the few atom case even if we relax the single photon excitation requirement. Let $\boldsymbol{E}_0\cos(\boldsymbol{k}_L\cdot\boldsymbol{x}-\omega_L t)$ is the field of the monochromatic excitation laser and σ_0 is scattering cross section of a single atom. For example, we find the radiated intensity in the 2-atom case for atoms with positions $\boldsymbol{x}_1$, $\boldsymbol{x}_2$,

$\boldsymbol{x}_{12} = \boldsymbol{x}_1 - \boldsymbol{x}_2$ in the weak field $\Omega \ll \gamma_0$ limit, $2\Omega = \boldsymbol{d} \cdot \boldsymbol{E}_0$, we have [67]

$$I = \sigma I_L \tag{5.7}$$

$$\begin{aligned}\sigma =& \sigma_0 \Bigg[\frac{\gamma_0(\gamma_0 + \gamma_{12})}{(\omega_L - (\omega_0 + \omega_{12}))^2 + (\gamma_0 + \gamma_{12})^2} \left[1 + \cos(\boldsymbol{k}_L \cdot \boldsymbol{x}_{12})\right] \\ &+ \frac{\gamma_0(\gamma_0 - \gamma_{12})}{(\omega_L - (\omega_0 - \omega_{12}))^2 + (\gamma_0 - \gamma_{12})^2} \left[1 - \cos(\boldsymbol{k}_L \cdot \boldsymbol{x}_{12})\right] \Bigg]\end{aligned} \tag{5.8}$$

Here the first term is superradiant emission, while the second is subradiant emission, and γ_{12} and ω_{12} are given by (4.23). For a line of classical oscillators in a phased match array, emission is enhanced in the phased match direction and suppressed otherwise. It has been shown that a similar effect emerges in the cooperative emission of N identical atoms as a requirement of energy conservation [6]. One may also employ the Lehmberg master equation to calculate photon statistics in the few atom case [26, 27].

5.1.2.1 Strongly driven atoms

For the case of a single atom strongly driven on resonance, we find a Mollow triplet [59]. It has been conjectured that in the very high power limit the N-atom case gives emission that is simply N-times the one atom case, recovering the Mollow triplet [2]. As we reduce the power, cooperative effects modify the triplet [16]. In our work, we will further numerically explore the effect of strongly driven multi-atom systems.

5.1.3 Acknowledgements

This chapter includes very significant amounts of work from undergraduate students I mentored over the course of writing this thesis. The work on directional emission was done with Songbo Xie (REU student). The work on the effect of high excitation power was done with Zihaui Zhang (REU student). I would like to thank them all for their extremely hard work in obtaining these results.

5.2 QuTiP toolbox for solving quantum master equation

The simulations on directional emission were performed using the QutiP python toolbox [40]. Our goal will be to solve a master equation of the density matrix [25]

$$\begin{aligned}\dot{\rho} =& -i\left[H_S,\rho\right]+\sum_{\alpha,\beta}\gamma_{\alpha\beta}\left[\sigma_\beta\rho\sigma_\alpha^\dagger-\frac{1}{2}\left(\rho\sigma_\alpha^\dagger\sigma_\beta+\sigma_\alpha^\dagger\sigma_\beta\rho\right)\right]\\ H_S =& \sum_\alpha\left(\omega_0-\Omega_{\alpha\alpha}\right)\sigma_\alpha^\dagger\sigma_\alpha+\sum_{\alpha\neq\beta}\Omega_{\alpha\beta}\sigma_\alpha^\dagger\sigma_\beta+H_L\\ H_L =& -\frac{1}{2}\sum_\alpha\left(\Omega_\alpha e^{i(\boldsymbol{k}\cdot\boldsymbol{r}_\alpha-\omega t)}\sigma_\alpha^\dagger+H.c.\right)\end{aligned} \tag{5.9}$$

Here $\Omega_{\alpha\alpha}$ is the Lamb shift of atom α and is assumed to be 0. $\Omega_\alpha := \boldsymbol{\mu}_\alpha\cdot\boldsymbol{E}$ is the Rabi frequency. QuTip solves master equations of the form

$$\dot{\rho} = -i\left[H(t),\rho(t)\right]+\sum_n\frac{1}{2}\left[2C_n\rho C_n^\dagger-\rho C_n^\dagger C_n-C_n^\dagger C_n\rho\right] \tag{5.10}$$

To make (5.9) look like (5.10) we need to define new operators that are linear combinations of σ_α that diagonalize the Hamiltonian,

$$A_\alpha = \sum_\beta u_{\beta\alpha}\sigma_\beta \tag{5.11}$$

This transforms 5.9 into

$$\dot{\rho} = -i\left[H,\rho\right]+\sum_\alpha\lambda_\alpha\left[A_\alpha\rho A_\alpha^\dagger-\frac{1}{2}\rho C_\alpha^\dagger C_\alpha-C_\alpha^\dagger C_\alpha\rho\right], \tag{5.12}$$

which is of the appropriate form. We then switch into the interaction picture to eliminate the time dependence on the laser field terms in H_L. The master equation can then by solved by the QuTiP toolbox by calling

$$\langle E_\beta(t)\rangle = \mathrm{mesolve}\left(H,\rho_0,\mathrm{timelist},C_\alpha,E_\beta(0)\right) \tag{5.13}$$

Here $E_\beta(t)$ are the expectation values of some operators, H is the Hamiltonian as in (5.10) , timelist is a list of times the program will use while solving, C_α are the collapse operators from (5.10).

To calculate intensity, we use [49],

$$I(t) = \sum_{\alpha,\beta} \gamma_{\alpha\beta} \langle \sigma^\dagger_\alpha(t) \sigma_\beta(t) \rangle. \tag{5.14}$$

5.2.1 Emission spectra

In order to calculate the emission spectra as a function of wavelength, we use

$$S(\omega) = \mathrm{Re}\left[\int_0^\infty \mathrm{d}t \int_0^\infty \mathrm{d}t' f(t,t') e^{-i\omega(t-t')}\right] \tag{5.15}$$

QuTiP can also solve multi-time expectation values using the quantum regression theorem. Practically,

$$\langle A(t+\tau)B(t)\rangle = \mathrm{correlation\_2op\_2t}(H, \rho_0, \mathrm{timelist1}, \mathrm{timelist2}, C_\alpha, A, B) \tag{5.16}$$

As shown in Fig. 5.1(a),(b) there is very good agreement between simulation and theory, they are almost perfectly overlapping. The additional delta like peak in the mollow triplet is due to elastic scattering [59].

5.3 Directional emission

One hallmark of superradiance is highly directional emission [86, 61]. A simple way to understand this is that the phenomenon of superradiance results from phase coherence between emitters, and carefully spaced in-phase dipoles will interfere constructively, which leads to the directionality.

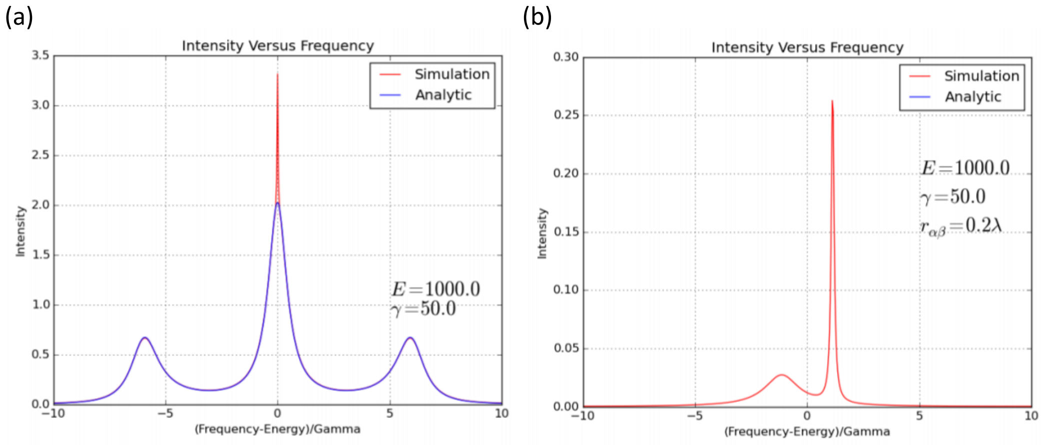

Figure 5.1: (a) Mollow triplet for a peak at 1 eV with decay rate 50 meV pumped with Rabi frequency 300 meV. (b) Super- and sub- radiant emission for a pair of atoms as in (a), separated by 0.2λ in 3 dimensions.

5.3.1 Directional emission: theory

We now have the tools to calculate the experimental signatures of superradiance: an N-fold increase in the spontaneous emission rate for closely spaced atoms, and highly directional emission when $N \gg 1$.

The angle-resolved emission intensity $I_{\hat{\boldsymbol{R}},d}(t)$ for a detector at position $\boldsymbol{R} = R\hat{\boldsymbol{R}}$ in dD is

$$I_{\hat{\boldsymbol{R}},d}(t) = \lim_{\Delta\Omega_{\hat{\boldsymbol{R}}}\to 0} \frac{1}{\Delta\Omega_{\hat{\boldsymbol{R}}}} \sum_{\boldsymbol{k}(\Delta\Omega_{\hat{\boldsymbol{R}}})l} \frac{\mathrm{d}}{\mathrm{d}t}\left\langle a^{\dagger}_{\boldsymbol{k}l}(t)\, a_{\boldsymbol{k}l}(t)\right\rangle \tag{5.17}$$

Theorem V.1. *For* $r_{\imath\jmath,max} \ll R$,

$$I_{\hat{\boldsymbol{R}},d}(t_R) = \sum_{\imath\jmath} w_{\hat{R},\imath\jmath}\, e^{ik_0\hat{\boldsymbol{R}}\cdot\boldsymbol{r}_{\imath\jmath}}\langle\hat{\sigma}_{\imath}^{\dagger}(t)\hat{\sigma}_{\jmath}(t)\rangle, \tag{5.18}$$

$$w_{\hat{R},\imath\jmath,d} =(2\pi)^{2-d}k_0^d\boldsymbol{\mu}_\imath\cdot\left[\mathbb{1}_3-\hat{\boldsymbol{R}}\hat{\boldsymbol{R}}\right]\cdot\boldsymbol{\mu}_\jmath. \tag{5.19}$$

Here $t_R = t + R/c$.

Proof. In (5.17), we first substitute $\hat{a}_{\boldsymbol{k}l}(t)$ by (4.6) and drop the $\hat{a}_{\boldsymbol{k}l}(0)$ terms since those correspond to the initial source of excitation. Then, in analogy with (4.8), we convert the sum over $\boldsymbol{k}$ into integration over ω as

$$\frac{1}{V}\lim_{\Delta\Omega_{\hat{\boldsymbol{R}}}\to 0}\frac{1}{\Delta\Omega_{\hat{\boldsymbol{R}}}}\sum_{\boldsymbol{k}(\Delta\Omega_{\hat{\boldsymbol{R}}})} \to \frac{1}{(2\pi c)^d}\int \mathrm{d}\omega\omega^{d-1}. \tag{5.20}$$

Also using (4.10), we obtain

$$\begin{aligned} I_{\hat{\boldsymbol{R}}}(t_R) =& 2\pi\sum_{\imath\jmath}\int \mathrm{d}\omega\left(\frac{\omega}{2\pi c}\right)^d \mathrm{e}^{\mathrm{i}\omega\hat{\boldsymbol{R}}\cdot\boldsymbol{r}_{\imath\jmath}/c} \\ & \times \boldsymbol{\mu}_\imath\cdot\left[\mathbb{1}_3 - \hat{\boldsymbol{R}}\hat{\boldsymbol{R}}\right]\cdot\boldsymbol{\mu}_\jmath & (5.21) \\ & \times\left[\int_0^t \mathrm{d}t'\hat{s}_\imath(t')\hat{s}_\jmath(t)\mathrm{e}^{-\mathrm{i}\omega(t'-t)}\right. \\ & \left. + \int_0^t \mathrm{d}t'\hat{s}_\imath(t)\hat{s}_\jmath(t')\mathrm{e}^{-\mathrm{i}\omega(t-t')}\right], & (5.22) \\ \hat{s}_\imath(t) =& \hat{\sigma}_\imath^\dagger(t) + \hat{\sigma}_\imath(t). & (5.23) \end{aligned}$$

Evaluating the integrals over t, the term in brackets becomes

$$2\pi\left[\delta(\omega+\omega_0)\hat{\sigma}_\imath(t)\hat{\sigma}_\jmath^\dagger(t) + \delta(\omega-\omega_0)\hat{\sigma}_\imath^\dagger(t)\hat{\sigma}_\jmath(t)\right]. \tag{5.24}$$

Integration over ω is trivial due to the δ-function, and comparing (5.18) and (5.21) completes the proof. This agrees with the previously derived 3D result [49]. □

The total spontaneous emission intensity as a function of time is obtained by integrating (5.18) over all angles:

$$\begin{aligned} I_d(t_R) &= \int \mathrm{d}^{d-1}\Omega_{\hat{\boldsymbol{R}}} I_{\hat{\boldsymbol{R}},d}(t_R) \\ &= \sum_{\imath\jmath} \gamma_{\imath\jmath} \langle \hat{\sigma}_\imath^\dagger(t)\hat{\sigma}_\jmath(t)\rangle, \end{aligned} \tag{5.25}$$

where $\gamma_{\imath\jmath}$ is the given in (4.4).

To examine the N-dependence of the directionality and intensity of the emission, we evaluate $I_{\hat{\boldsymbol{R}}}(t_R)$ and $I_d(t_R)$ explicitly. We consider the simplified case where there is no external field and the atoms are initialized into the symmetric state $|S_N\rangle$:

$$|S_N\rangle = \frac{1}{\sqrt{N}} \sum_{\imath=1}^{N} |g\rangle_1 \cdots |e\rangle_\imath \cdots |g\rangle_N \tag{5.26}$$

For this initial condition $\rho_{S_N,S_N}(0) = |S_N\rangle\langle S_N| = 1$ and all other density matrix elements are 0. For later times we assume

$$\rho_{S_N,S_N}(t) = \mathrm{e}^{-\gamma_{S_N} t}, \tag{5.27}$$

and that the other density matrix elements remain 0, where γ_{S_N} is the spontaneous emission rate of state $|S_N\rangle$. In the Dicke limit this result is exact, with $\gamma_{S_N} = N\gamma_{\imath\imath}$. This assumption is a reasonable approximation for closely spaced atoms with $k_0 r_{\imath\jmath,\max} \ll 1$. For these initial conditions

$$\langle \hat{\sigma}_\imath^\dagger(t)\hat{\sigma}_\jmath(t)\rangle = \frac{1}{N}\rho_{S_N,S_N}(t), \tag{5.28}$$

For parallel dipoles we have,

$$\begin{aligned} I_{\hat{\boldsymbol{R}},d}(t_R) =& I_{\hat{\boldsymbol{R}},d,1}(t_R)\frac{\mathrm{e}^{-(\gamma_{S_N}-\gamma)t}}{N} \\ & \times \sum_{\imath,\jmath} \cos\left(k_0 \hat{\boldsymbol{R}} \cdot \boldsymbol{r}_{\imath\jmath}\right), \end{aligned} \tag{5.29}$$

$$I_{\hat{\boldsymbol{R}},d,1}(t_R) = w_{\hat{R},\imath,d}\mathrm{e}^{-\gamma t}. \tag{5.30}$$

Here $I_{\hat{\boldsymbol{R}},d,1}(t_R)$ is the angle-resolved intensity from a single atom. Hence $I_{\hat{\boldsymbol{R}},d}(t_R)$ consist of N^2 terms that are proportional to the single-atom spontaneous emission, with the cosine factor of each term resulting in an interference effect. This results shows that the collective emission of the atoms in the far field is analogous to that of a phased antenna array of classical dipoles. The dimensional dependence is the same as that of a single atom.

To examine the emergence of directionality, we consider a pencil shaped array of emitters with equal spacing L, or

$$\boldsymbol{r}_{\imath\jmath} = (\jmath - \imath)L\hat{\boldsymbol{L}}. \tag{5.31}$$

Using (5.29) we obtain

$$I_{\theta,d}(t_R) = I_{\theta,d,1}(t_R)\frac{\mathrm{e}^{-(\gamma_{S_N}-\gamma)t}}{N}\frac{\sin^2(Nk_0 L\cos\theta/2)}{\sin^2(k_0 L\cos\theta/2)}, \tag{5.32}$$

for $\cos\theta = \hat{\boldsymbol{R}} \cdot \hat{\boldsymbol{L}}$. As N increases, the emission becomes increasingly directional, consistent with earlier results for 3D [14].

Integrating over all solid angles we find the total emitted intensity,

$$I(t_R) = \gamma_{S_N}\mathrm{e}^{-\gamma_{S_N}t}\,, \gamma_{S_N} = \sum_{\imath\jmath}\frac{\gamma_{\imath\jmath}}{N} \tag{5.33}$$

This shows the N-fold increase in the spontaneous emission rate for closely spaced

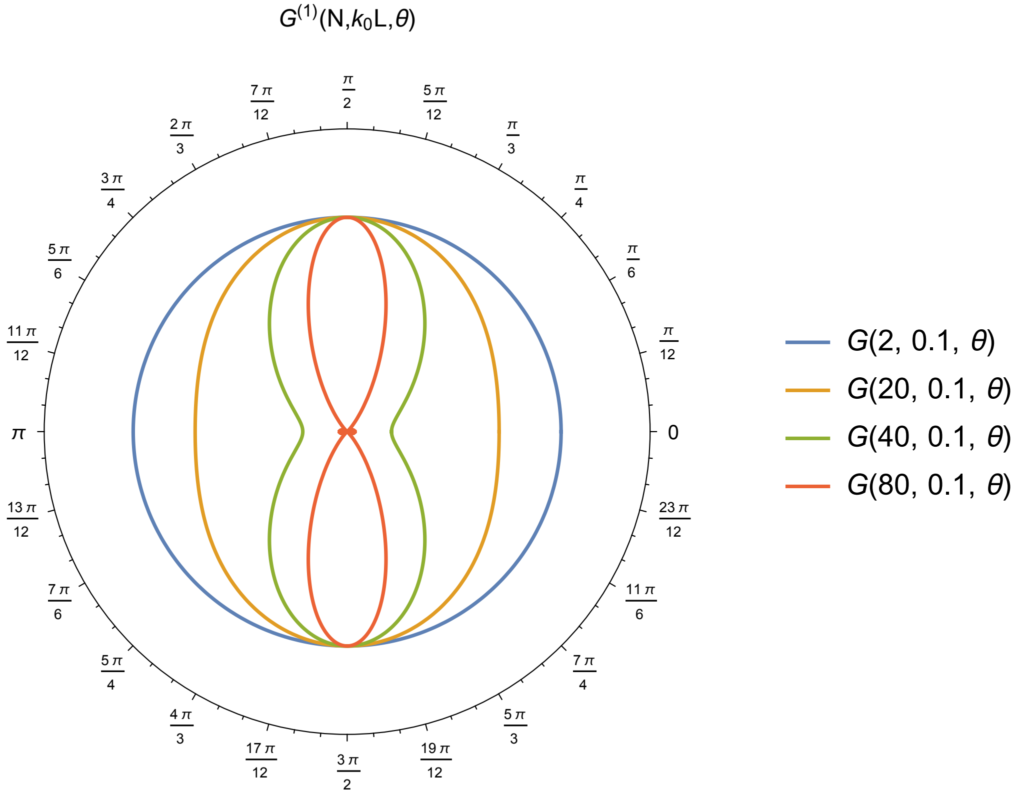

Figure 5.2: We define the normalized intensity $G^{(1)}(N, k_0L, \theta) = \frac{1}{N} G^{(1)}_{\theta,d}(0,0)$ using (5.32), from atoms in a line with spacing $k_0L = 0.1$.

atoms, independent of dimension.

5.3.2 Directional emission: QuTiP simulation

We can also simulate directional emission for atoms with spacing $k_0 L = 0.1$. The exact solution has expontential computational cost in the number of atoms, so we are limited to simulation of up to 9 atoms with this method. However, the emergence of directional emission is clearly visible, and matches very well with the analytic prediction (5.32) of increasing directionality with the number of atoms.

5.4 Generalizing the Mollow triplet

A single atom strongly interacting with the electromagnetic field results in a mollow triplet, as shown in Fig. 5.1(a). The usual explanation is that the strong field “dresses’ the bare states, resulting in three peaks as shown in Fig. 5.4. We seek to explore numerically and quantitatively what occurs when we have a system exhibiting superradiance and subject it to an intense optical driving field. When two atoms are sufficiently close, they may exchange photons often enough to split the emission mode into symmetric and antisymmetric emission modes, referred to as a super- and subradiant emission. This occurs when the atoms are strongly coupled to each other. The mollow triplet occurs when individual atoms are strongly coupled to the field. As a result, at low power, we will see the super- and sub-radiant emission, as expected. At sufficiently high power, the coupling to the intense driving field will be stronger than the super-radiant coupling, and the emission will return to exhibiting a single mollow triplet. At intermediate power, when the coupling to the driving field and the coupling to each other through cooperative scattering are comparable, we expect that the field will dress the super- and sub- radiant modes, resulting in a complex emission pattern with many peaks. This is quantitatively what we see via simulation.

In Fig. 5.5(a) we see that at low driving power, the split between the super- and

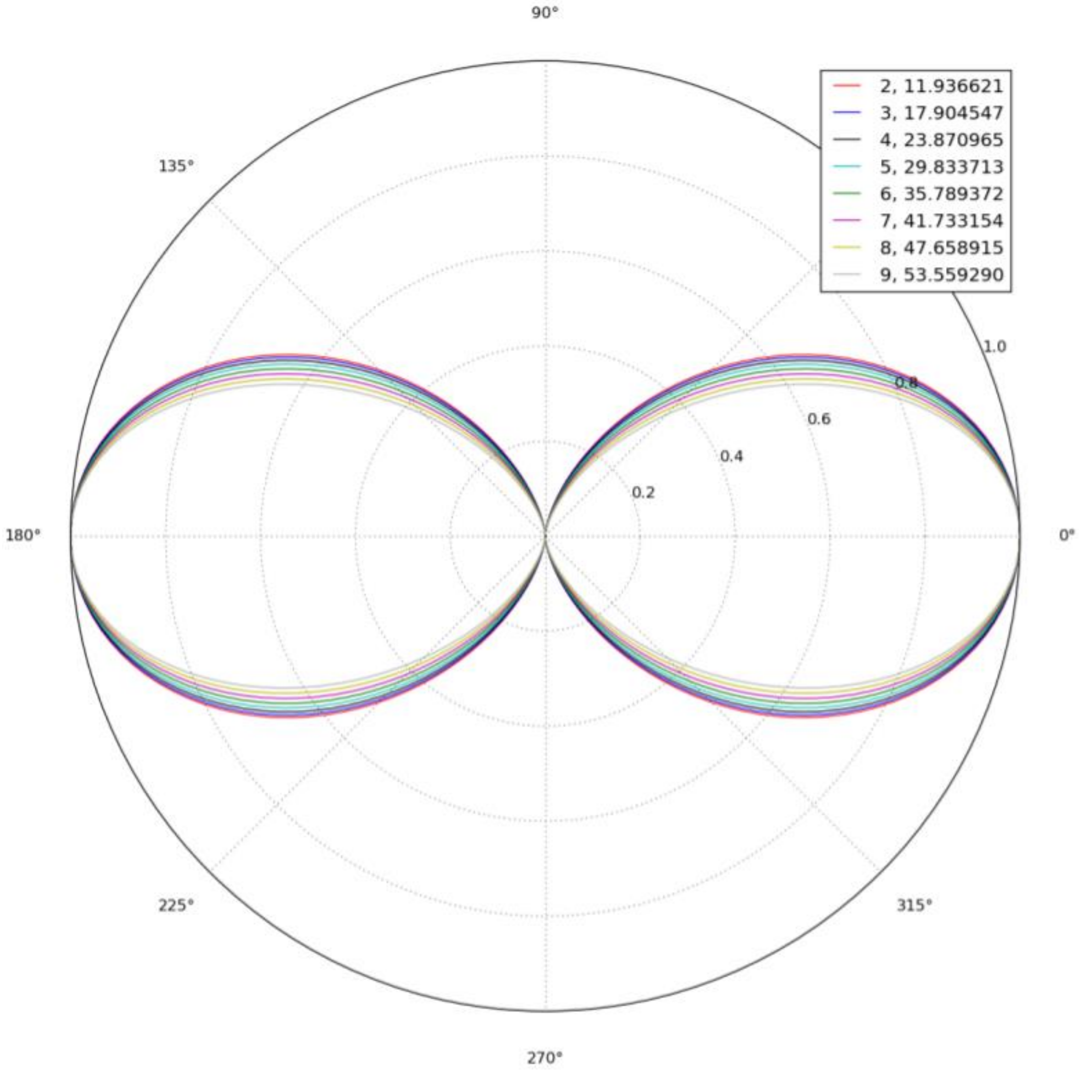

Figure 5.3: This shows 2 through 9 atoms spaced in a line with $k_0L = 0.1$ spacing. The emission is normalized to 1 at 0 degrees.

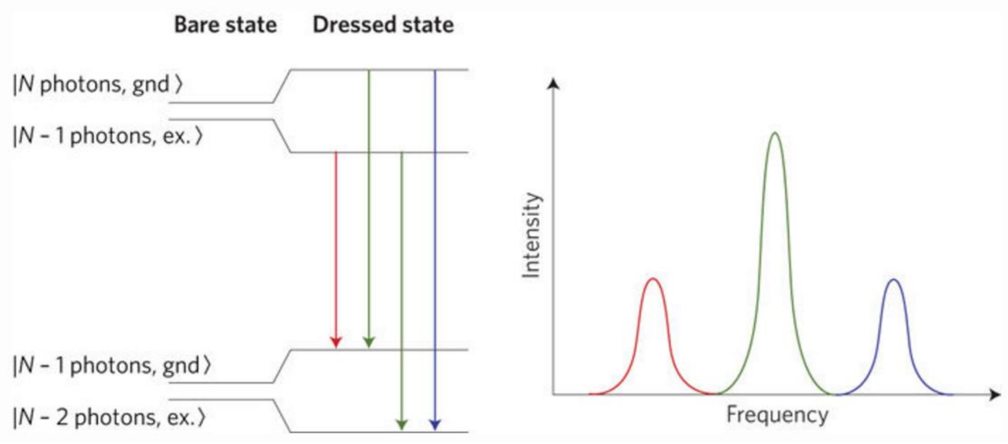

Figure 5.4: Explanation of mollow triplet in terms of dressed state picture. Image taken from [71].

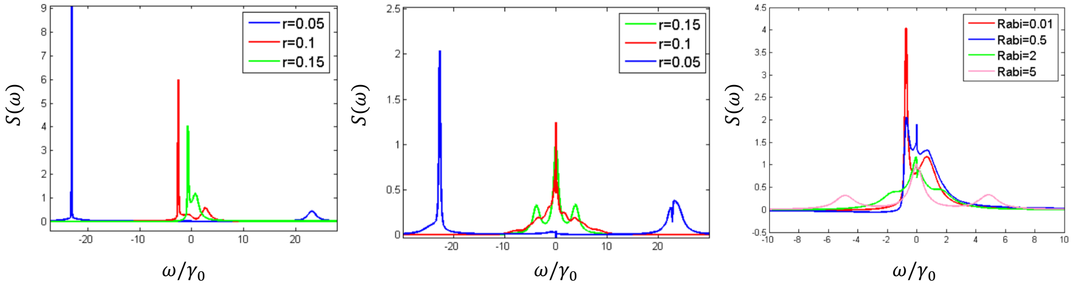

Figure 5.5: (a) two atoms spaced $r = 0.05\lambda, 0.1\lambda, 0.15\lambda$ excited with lower power $\Omega_{\text{Rabi}} \ll 1$ (b) Same atom spacing as (a) but with $\Omega_{\text{Rabi}} > 1$ (c) two atoms with $r = 0.15\lambda$ spacing and varying excitation power.

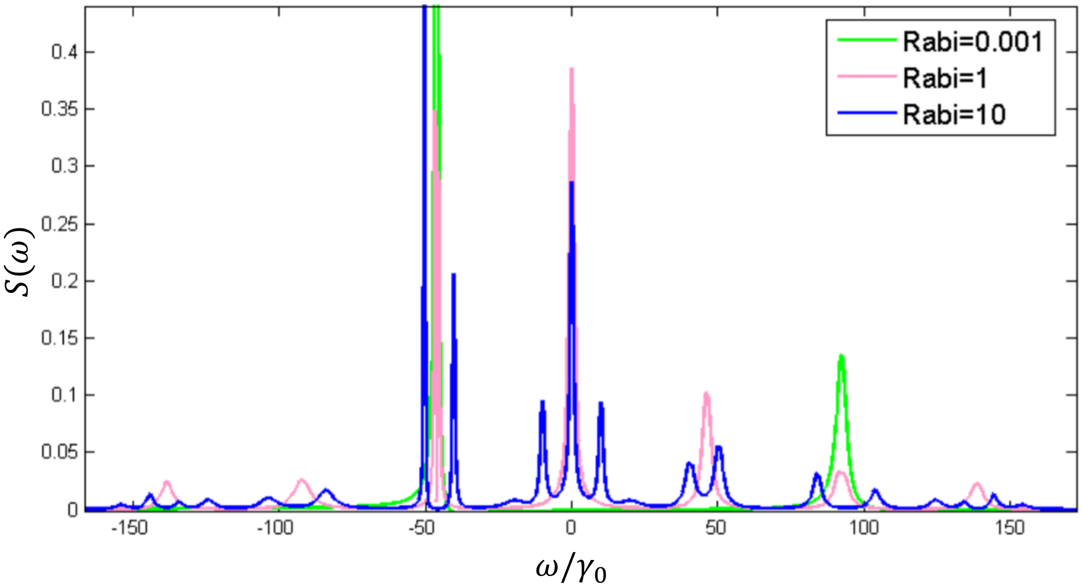

Figure 5.6: Here we have 3 very closely spaced atoms arranged in an equilateral triangle such that $\omega_{12} = \omega_{13} = \omega_{23} \approx 50\gamma_0$, and very the driving field.

sub- radiant peak increases as the photon mediated coupling increases with decreasing atomic separation. In Fig. 5.5(b) the peak position is approximately the same for the closest atom spacing, but as the atoms are placed further apart the coupling to the field wins out and the mollow triplet is recovered. In Fig. 5.5(c) the spacing is fixed and as we increase the driving field, the super- and sub- radiant peaks collapse before the emergence of the usual mollow sidebands.

For the case of three atoms in an equilateral triangle with very close spacing such that $\omega_{12} \approx 50\gamma_0$, γ_0 the single atom decay rate, we see an extremely complicated dependence of the emission spectra on driving field. At very low power there are two peaks at $\omega - \omega_{12}$ and $\omega + 2\omega_{12}$ as expected. As power is increased, additional peaks appear with spacing between them approximately spaced $\omega_{12} \approx 50\gamma_0$. As power is further increased, these individual peaks split into two to four peaks, with splitting on the order of the driving field frequency.

5.5 Superradiance in a two dimensional atomic gas

The master equation for an atomic operator in an N atom system can be written in matrix form as

$$\dot{Q} = i\left[\tilde{\sigma}^{\dagger}\tilde{\omega}\tilde{\sigma}^{T}, Q\right] + \left(\tilde{\sigma}^{\dagger}\tilde{\gamma}Q\tilde{\sigma}^{T} - \frac{1}{2}\tilde{\sigma}^{\dagger}\tilde{\gamma}\tilde{\sigma}^{T}Q - \frac{1}{2}Q\tilde{\sigma}^{\dagger}\tilde{\gamma}\tilde{\sigma}^{T}\right) \tag{5.34}$$

Here $\tilde{\sigma}$ is an N element row vector with i^{th} element $\sigma_i = |-\rangle_{ii}\langle -|$. $\tilde{\omega}$ and $\tilde{\gamma}$ are $N \times N$ matrices with entires that satisfy, for two dimensional dipoles oriented perpendicular to the plane of confinement,

$$\tilde{\Gamma}_{\imath\jmath} := -\tilde{\omega}_{\imath\jmath} + \frac{i}{2}\tilde{\gamma}_{\imath\jmath} = \frac{i\gamma_0}{2}H_0^{(1)}(k_0 r_{\imath\jmath}). \tag{5.35}$$

The eigenvalues of $\tilde{\gamma}$ give the decay rates of the system, with the largest decay rate the most strongly superradiant mode. Here we investigate how the largest eigenvalue of the system, which we label γ_1, scales with the size and density of a two dimensional atomic gas.

Fig. 5.7(c) implies γ_1 has a power law relationship with the density

$$\gamma_1 \propto \rho^{\beta}. \tag{5.36}$$

For a lattice, we expect $\beta \approx 0.5$ [53]. We find from Fig. 5.7(c) that for $\rho > 1\text{atom}/(\lambda/2\pi)^2$, $\beta \approx 0.45$.

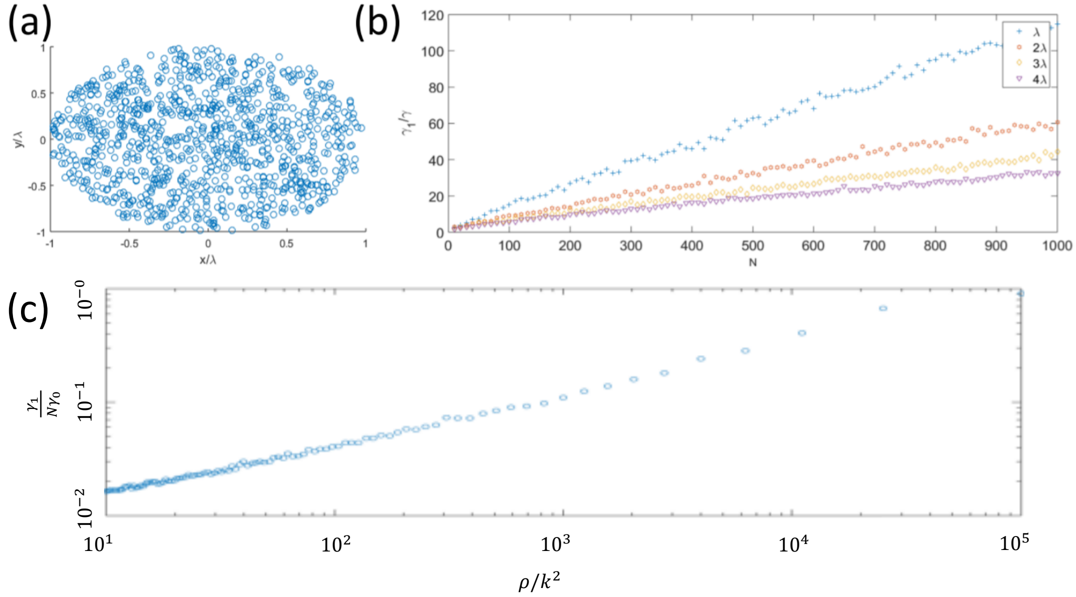

Figure 5.7: (a) 1000 atoms randomly placed in a cirle of radius equal to λ. (b) shows γ_1, the largest superradiant eigenvalue, as a function of number of atoms in a circle of radii $r = \lambda, 2\lambda, 3\lambda, 4\lambda$. (c) plot of γ as a function of density on a log-log plot.

CHAPTER VI

Conclusions

How does geometry affect the spontaneous emission properties of a two level system? We obtained the following results:

In chapter 2 we find the radiative enhancement in the quasi-static approximation of a dipole placed in 'wire' that consists of an arbitrary number of infinite concentric dielectric cylinders. Our solution is a simle closed-form result We predicted over 1000-fold enhancement of the radiative emission rate for GaN-Silver plasmonic resonance near the 435nm, even in the presecence of a Al_2O_3 spacer layer. The addition of the spacer layer has relatively minimal effect on radiative enhancement, but significantly decreases the non-radiative enhancement based on scaling argument. We obtain a series solution for the non-radiative emission rate for the same case of a wire consisting of concentric cylinders.

In chapter 3 we experimentally demonstrate radiative enhancement via plasmonic coupling of a InGaN quantum dot single photon source embedded in a GaN pillar surrounded by a conformal coating of silver with an Al_2O_3 spacer layer. The quantum dot is at the tip of a truncated cylinder. We demonstrate the enhancement is radiative by showing over order of magnitude enhancement of the photoluminescence intensity in conjunction with an even greater enhancement of the emission lifetime which contains both radiative and non-radiative components. We verify that the plasmonic coupling does not destroy the single photon source property by showing second order correlation $g^{(2)} < 0.5$ before and after the addition of the silver cavity.

In chapter 4 we examine cooperative light scattering changes as a function of the dimension of the system. We develop a formalism that unifies the treatment of cooperative effects in an open line, open plane, and open space appear. Our results are some of the earliest to fully describe the two dimensional case [55]. We examine the changes in the cooperative scattering in the asymptotic limits where the expressions take on particularly simple form. Furthermore, we discuss a potential implementation involving silicon vacancy centers in diamond in the nascent field of superradience in two dimensions.

In chapter 5 we demonstrate that the cooperative scattering effects we outlined in the previous chapter lead to the signatures of superradiance - enhanced spontaneous emission rate proportional to the number of 'atoms' contributing to the emission, and enhanced directionality of the emission. We present simulation results for enhanced directionality for an exact solution of atoms in a line with two dimensional coupling for up to 9 atoms, and have close agreement with a simple analytic result we derive. We examine how the spontaneous emission of the superradiant mode scales with density for a dilute two dimensional case, obtaining evidence of a clear power law relationship with density. The scaling power of 0.45 is similar to the power of 0.5 recently predicted for a regularly spaced infinite square lattice in two dimensions [53]. We furthermore examine computationally the interplay between the cooperative mode effects of superradiance and the effects of an ultra-high intensity excitation field, finding rich and complex behavior when the superradiant coupling and the coupling of individual 'atoms' to the field are of similar magnitude.

BIBLIOGRAPHY

BIBLIOGRAPHY

[1] A. V. Akimov, A. Mukherjee, C. L. Yu, D. E. Chang, A. S. Zibrov, P. R. Hemmer, H. Park, and M. D. Lukin. Generation of single optical plasmons in metallic nanowires coupled to quantum dots. *Nature*, 450(7168):402–406, Nov 2007.

[2] A. S. Jahangir Amin and J. G. Cordes. Multiatom effects in resonance fluorescence. *Phys. Rev. A*, 18:1298–1301, Sep 1978.

[3] A. S. Barker and M. Ilegems. Infrared lattice vibrations and free-electron dispersion in gan. *Phys. Rev. B*, 7:743–750, Jan 1973.

[4] Stephen M. Barnett, Bruno Huttner, and Rodney Loudon. Spontaneous emission in absorbing dielectric media. *Phys. Rev. Lett.*, 68:3698–3701, Jun 1992.

[5] L. Bellando, A. Gero, E. Akkermans, and R. Kaiser. Cooperative effects and disorder: A scaling analysis of the spectrum of the effective atomic hamiltonian. *Phys. Rev. A*, 90:063822, Dec 2014.

[6] P. R. Berman. Energy conservation in collective coherent emission by dipole oscillators. *American Journal of Physics*, 78(12):1323–1330, 2010.

[7] Justin G. Bohnet, Zilong Chen, Joshua M. Weiner, Dominic Meiser, Murray J. Holland, and James K. Thompson. A steady-state superradiant laser with less than one intracavity photon. *Nature*, 484(7392):78–81, 04 2012.

[8] X. Brokmann, L. Coolen, M. Dahan, and J. P. Hermier. Measurement of the radiative and nonradiative decay rates of single cdse nanocrystals through a controlled modification of their spontaneous emission. *Phys. Rev. Lett.*, 93:107403, Sep 2004.

[9] Iulia Buluta, Sahel Ashhab, and Franco Nori. Natural and artificial atoms for quantum computation. *Reports on Progress in Physics*, 74(10):104401, 2011.

[10] RR Chance, A Prock, and R Silbey. Molecular fluorescence and energy transfer near interfaces. *Adv. Chem. Phys*, 37(1):65, 1978.

[11] Darrick E. Chang, Anders S. Sø rensen, Eugene A. Demler, and Mikhail D. Lukin. A single-photon transistor using nanoscale surface plasmons. *Nat. Phys.*, 3(11):807–812, August 2007.

[12] H. Chew. Radiation and lifetimes of atoms inside dielectric particles. *Phys. Rev. A*, 38:3410–3416, Oct 1988.

[13] Jennifer T. Choy, Birgit J. M. Hausmann, Thomas M. Babinec, Irfan Bulu, Mughees Khan, Patrick Maletinsky, Amir Yacoby, and Marko Loncar. Enhanced single-photon emission from a diamond-silver aperture. *Nat Photon*, 5(12):738–743, Dec 2011.

[14] J. P. Clemens, L. Horvath, B. C. Sanders, and H. J. Carmichael. Collective spontaneous emission from a line of atoms. *Phys. Rev. A*, 68:023809, Aug 2003.

[15] Ph W Courteille, Simone Bux, Eleonora Lucioni, Katharina Lauber, Tom Bienaime, Robin Kaiser, and Nicola Piovella. Modification of radiation pressure due to cooperative scattering of light. *The European Physical Journal D-Atomic, Molecular, Optical and Plasma Physics*, 58(1):69–73, 2010.

[16] Sumanta Das, G. S. Agarwal, and Marlan O. Scully. Quantum interferences in cooperative dicke emission from spatial variation of the laser phase. *Phys. Rev. Lett.*, 101:153601, Oct 2008.

[17] M De Vittorio, Ferruccio Pisanello, L Martiradonna, Antonio Qualtieri, Tiziana Stomeo, A Bramati, and R Cingolani. Recent advances on single photon sources based on single colloidal nanocrystals. 18:1–9, 03 2010.

[18] Brandon Demory, Tyler A. Hill, Chu-Hsiang Teng, Lei Zhang, Hui Deng, and Pei-Cheng Ku. Plasmonic enhancement of single photon emission from a site-controlled quantum dot. *ACS Photonics*, 2(8):1065–1070, 2015.

[19] R. G. DeVoe and R. G. Brewer. Observation of Superradiant and Subradiant Spontaneous Emission of Two Trapped Ions. *Phys. Rev. Lett.*, 76(12):2049–2052, March 1996.

[20] Robert Henry Dicke. Coherence in spontaneous radiation processes. *Phys. Rev.*, 93:99–110, Jan 1954.

[21] Karl H Drexhage. Monomolecular layers and light. *Scientific American*, 222(3):108–120, 1970.

[22] David Dzsotjan, Anders S. Sørensen, and Michael Fleischhauer. Quantum emitters coupled to surface plasmons of a nanowire: A green's function approach. *Phys. Rev. B*, 82:075427, Aug 2010.

[23] V. Ernst. Coherent emission of a photon by many atoms. *Zeitschrift für Physik*, 218(2):111–128, Apr 1969.

[24] Enrico Fermi. Quantum theory of radiation. *Rev. Mod. Phys.*, 4:87–132, Jan 1932.

[25] Z. Ficek and R. Tana. Entangled states and collective nonclassical effects in two-atom systems. *Physics Reports*, 372(5):369 – 443, 2002.

[26] Z. Ficek, R. Tanaś, and S. Kielich. Photon antibunching and squeezing in resonance fluorescence of two interacting atoms. *Phys. Rev. A*, 29:2004–2011, Apr 1984.

[27] Zbigniew Ficek and Barry C. Sanders. Quantum beats in two-atom resonance fluorescence. *Phys. Rev. A*, 41:359–368, Jan 1990.

[28] R. Friedberg, S.R. Hartmann, and J.T. Manassah. Frequency shifts in emission and absorption by resonant systems ot two-level atoms. *Physics Reports*, 7(3):101 – 179, 1973.

[29] Richard Friedberg and Jamal T. Manassah. Effects of including the counterrotating term and virtual photons on the eigenfunctions and eigenvalues of a scalar photon collective emission theory. *Physics Letters A*, 372(14):2514 – 2521, 2008.

[30] D. P. Fussell, R. C. McPhedran, and C. Martijn de Sterke. Three-dimensional green's tensor, local density of states, and spontaneous emission in finite two-dimensional photonic crystals composed of cylinders. *Phys. Rev. E*, 70:066608, Dec 2004.

[31] A. González-Tudela, C.-L. Hung, D. E. Chang, J. I. Cirac, and H. J. Kimble. Subwavelength vacuum lattices and atomatom interactions in two-dimensional photonic crystals. *Nature Photonics*, 9(5):320–325, 5 2015.

[32] A. González-Tudela, D. Martin-Cano, E. Moreno, L. Martin-Moreno, C. Tejedor, and F. J. Garcia-Vidal. Entanglement of Two Qubits Mediated by One-Dimensional Plasmonic Waveguides. *Phys. Rev. Lett.*, 106(2):020501, January 2011.

[33] Xing-Fei He. Excitons in anisotropic solids: The model of fractional-dimensional space. *Phys. Rev. B*, 43:2063–2069, Jan 1991.

[34] K. Hennessy, A. Badolato, M. Winger, D. Gerace, M. Atature, S. Gulde, S. Falt, E. L. Hu, and A. Imamoglu. Quantum nature of a strongly coupled single quantum dot-cavity system. *Nature*, 445(7130):896–899, Feb 2007.

[35] Tyler Hill, Barry C. Sanders, and Hui Deng. Cooperative light scattering in any dimension. *Phys. Rev. A*, 95:033832, Mar 2017.

[36] Carrie E. Hofmann, F. Javier Garca de Abajo, and Harry A. Atwater. Enhancing the radiative rate in iiiv semiconductor plasmonic coreshell nanowire resonators. *Nano Letters*, 11(2):372–376, 2011. PMID: 21244054.

[37] Mark J. Holmes, Kihyun Choi, Satoshi Kako, Munetaka Arita, and Yasuhiko Arakawa. Room-temperature triggered single photon emission from a iii-nitride site-controlled nanowire quantum dot. *Nano Letters*, 14(2):982–986, 2014. PMID: 24422516.

[38] Zubin Jacob, Igor I Smolyaninov, and Evgenii E Narimanov. Broadband purcell effect: Radiative decay engineering with metamaterials. *Applied Physics Letters*, 100(18):181105, 2012.

[39] F. Jelezko and J. Wrachtrup. Single defect centres in diamond: A review. *physica status solidi (a)*, 203(13):3207–3225, 2006.

[40] J.R. Johansson, P.D. Nation, and Franco Nori. Qutip 2: A python framework for the dynamics of open quantum systems. *Computer Physics Communications*, 184(4):1234 – 1240, 2013.

[41] P. B. Johnson and R. W. Christy. Optical constants of the noble metals. *Phys. Rev. B*, 6:4370–4379, Dec 1972.

[42] Satoshi Kako, Charles Santori, Katsuyuki Hoshino, Stephan Gtzinger, Yoshihisa Yamamoto, and Yasuhiko Arakawa. A gallium nitride single-photon source operating at 200k. 5:887–92, 12 2006.

[43] AV Karnyukhin, RN Kuz'min, and VA Namiot. Superradiance in a two-dimensional model. *Sov. Phys.-JETP*, 57:509–517, 1983.

[44] V. V. Klimov and M. Ducloy. Spontaneous emission rate of an excited atom placed near a nanofiber. *Phys. Rev. A*, 69:013812, Jan 2004.

[45] Jasper Knoester and Shaul Mukamel. Intermolecular forces, spontaneous emission, and superradiance in a dielectric medium: Polariton-mediated interactions. *Phys. Rev. A*, 40:7065–7080, Dec 1989.

[46] W. J. M. Kort-Kamp, F. S. S. Rosa, F. A. Pinheiro, and C. Farina. Spontaneous emission in the presence of a spherical plasmonic metamaterial. *Phys. Rev. A*, 87:023837, Feb 2013.

[47] Kevin Lalumière, Barry C. Sanders, A. F. van Loo, A. Fedorov, A. Wallraff, and A. Blais. Input-output theory for waveguide QED with an ensemble of inhomogeneous atoms. *Phys. Rev. A*, 88(4):043806, October 2013.

[48] Leung Kway Lee and P.-C. Ku. Fabrication of site-controlled ingan quantum dots using reactive-ion etching. *physica status solidi (c)*, 9(3-4):609–612, 2012.

[49] R. H. Lehmberg. Radiation from an n-atom system. i. general formalism. *Phys. Rev. A*, 2:883–888, Sep 1970.

[50] L.-W. Li, M.-S. Leong, T.-S. Yeo, and P.-S. Kooi. Electromagnetic dyadic green's functions in spectral domain for multilayered cylinders. *Journal of Electromagnetic Waves and Applications*, 14(7):961–985, 2000.

[51] Le-Wei Li, Pang-Shyan Kooi, Mook-Seng Leong, and Tat-Soon Yee. Electromagnetic dyadic green's function in spherically multilayered media. *IEEE Transactions on Microwave Theory and Techniques*, 42(12):2302–2310, Dec 1994.

[52] D. A. Lidar, I. L. Chuang, and K. B. Whaley. Decoherence-free subspaces for quantum computation. *Phys. Rev. Lett.*, 81:2594–2597, Sep 1998.

[53] Paolo Longo, Christoph H. Keitel, and Jörg Evers. Tailoring superradiance to design artificial quantum systems. 6:23628 EP –, Mar 2016. Article.

[54] B Lounis and W E Moerner. Single photons on demand from a single molecule at room temperature. *Nature*, 407(6803):491–3, 2000.

[55] C. E. Máximo, N. Piovella, Ph. W. Courteille, R. Kaiser, and R. Bachelard. Spatial and temporal localization of light in two dimensions. *Phys. Rev. A*, 92:062702, Dec 2015.

[56] Z. Meir, O. Schwartz, E. Shahmoon, D. Oron, and R. Ozeri. Cooperative Lamb Shift in a Mesoscopic Atomic Array. *Phys. Rev. Lett.*, 113(19):193002, November 2014.

[57] Peter W. Milonni and Peter L. Knight. Retardation in the resonant interaction of two identical atoms. *Phys. Rev. A*, 10:1096–1108, Oct 1974.

[58] Yevhen Miroshnychenko, Uffe V. Poulsen, and Klaus Mølmer. Directional emission of single photons from small atomic samples. *Phys. Rev. A*, 87:023821, Feb 2013.

[59] B. R. Mollow. Power spectrum of light scattered by two-level systems. *Phys. Rev.*, 188:1969–1975, Dec 1969.

[60] H. MORAWITZ. Self-coupling of a two-level system by a mirror. *Phys. Rev.*, 187:1792–1796, Nov 1969.

[61] S. Oppel, R. Wiegner, G. S. Agarwal, and J. von Zanthier. Directional superradiant emission from statistically independent incoherent nonclassical and classical sources. *Phys. Rev. Lett.*, 113:263606, Dec 2014.

[62] Afaq Habib Piracha, Kumaravelu Ganesan, Desmond W. M. Lau, Alastair Stacey, Liam P. McGuinness, Snjezana Tomljenovic-Hanic, and Steven Prawer. Scalable fabrication of high-quality, ultra-thin single crystal diamond membrane windows. *Nanoscale*, 8:6860–6865, 2016.

[63] D. Porras and J. I. Cirac. Collective generation of quantum states of light by entangled atoms. *Phys. Rev. A*, 78:053816, Nov 2008.

[64] E. Prodan, C. Radloff, N. J. Halas, and P. Nordlander. A hybridization model for the plasmon response of complex nanostructures. *Science*, 302(5644):419–422, 2003.

[65] Edward Mills Purcell. Proc. am. phys. soc. *Phys. Rev.*, 69:674–674, Jun 1946.

[66] V. S. C. Manga Rao and S. Hughes. Single quantum dot spontaneous emission in a finite-size photonic crystal waveguide: Proposal for an efficient "on chip" single photon gun. *Phys. Rev. Lett.*, 99:193901, Nov 2007.

[67] Th. Richter. Cooperative resonance fluorescence from two atoms experiencing different driving fields. *Optica Acta: International Journal of Optics*, 30(12):1769–1780, 1983.

[68] L. J. Rogers, K. D. Jahnke, T. Teraji, L. Marseglia, C. Muller, B. Naydenov, H. Schauffert, C. Kranz, J. Isoya, L. P. McGuinness, and F. Jelezko. Multiple intrinsically identical single-photon emitters in the solid state. *Nat. Commun.*, 5:4739, 2014.

[69] Kasey J. Russell, Tsung-Li Liu, Shanying Cui, and Evelyn L. Hu. Large spontaneous emission enhancement in plasmonic nanocavities. *Nat Photon*, 6(7):459–462, Jul 2012.

[70] C Santori, P E Barclay, K-M C Fu, R G Beausoleil, S Spillane, and M Fisch. Nanophotonics for quantum optics using nitrogen-vacancy centers in diamond. *Nanotechnology*, 21(27):274008, July 2010.

[71] Charles Santori and Yoshihisa Yamamoto. Quantum dots: Driven to perfection. *Nat Phys*, 5(3):173–174, Mar 2009.

[72] M. Schukraft, J. Zheng, T. Schrder, S. L. Mouradian, M. Walsh, M. E. Trusheim, H. Bakhru, and D. R. Englund. Invited article: Precision nanoimplantation of nitrogen vacancy centers into diamond photonic crystal cavities and waveguides. *APL Photonics*, 1(2), 2016.

[73] A. Sipahigil, R. E. Evans, D. D. Sukachev, M. J. Burek, J. Borregaard, M. K. Bhaskar, C. T. Nguyen, J. L. Pacheco, H. A. Atikian, C. Meuwly, R. M. Camacho, F. Jelezko, E. Bielejec, H. Park, M. Lončar, and M. D. Lukin. An integrated diamond nanophotonics platform for quantum-optical networks. *Science*, 354(6314):847–850, 2016.

[74] S. E. Skipetrov and I. M. Sokolov. Absence of anderson localization of light in a random ensemble of point scatterers. *Phys. Rev. Lett.*, 112:023905, Jan 2014.

[75] Frank H. Stillinger. Axiomatic basis for spaces with noninteger dimension. *J. Math. Phys.*, 18(6):1224, 1977.

[76] Anatoly Svidzinsky and Jun-Tao Chang. Cooperative spontaneous emission as a many-body eigenvalue problem. *Phys. Rev. A*, 77(4):043833, April 2008.

[77] Anatoly A. Svidzinsky. Nonlocal effects in single-photon superradiance. *Phys. Rev. A*, 85:013821, Jan 2012.

[78] Anatoly A. Svidzinsky, Jun-Tao Chang, and Marlan O. Scully. Dynamical evolution of correlated spontaneous emission of a single photon from a uniformly excited cloud of n atoms. *Phys. Rev. Lett.*, 100:160504, Apr 2008.

[79] Anatoly A. Svidzinsky, Jun-Tao Chang, and Marlan O. Scully. Cooperative spontaneous emission of n atoms: Many-body eigenstates, the effect of virtual lamb shift processes, and analogy with radiation of n classical oscillators. *Phys. Rev. A*, 81:053821, May 2010.

[80] Ph. Tamarat, T. Gaebel, J. R. Rabeau, M. Khan, A. D. Greentree, H. Wilson, L. C. L. Hollenberg, S. Prawer, P. Hemmer, F. Jelezko, and J. Wrachtrup. Stark Shift Control of Single Optical Centers in Diamond. *Phys. Rev. Lett.*, 97(8):083002, August 2006.

[81] Aniwat Tandaechanurat, Satomi Ishida, Denis Guimard, Masahiro Nomura, Satoshi Iwamoto, and Yasuhiko Arakawa. Lasing oscillation in a three-dimensional photonic crystal nanocavity with a complete bandgap. *Nat Photon*, 5(2):91–94, Feb 2011.

[82] Ye Tao and Christian Degen. Facile fabrication of single-crystal-diamond nanostructures with ultrahigh aspect ratio. *Adv. Mater.*, 25(29):3962–3967, 2013.

[83] David M Toyli, Christoph D Weis, Gregory D Fuchs, Thomas Schenkel, and David D Awschalom. Chip-scale nanofabrication of single spins and spin arrays in diamond. *Nano Lett.*, 10(8):3168–72, August 2010.

[84] Arjan F. van Loo, Arkady Fedorov, Kevin Lalumière, Barry C. Sanders, Alexandre Blais, and Andreas Wallraff. Photon-mediated interactions between distant artificial atoms. *Science*, 342(6165):1494–1496, 2013.

[85] JAE Wasey and WL Barnes. Efficiency of spontaneous emission from planar microcavities. *Journal of Modern Optics*, 47(4):725–741, 2000.

[86] R. Wiegner, J. von Zanthier, and G. S. Agarwal. Quantum-interference-initiated superradiant and subradiant emission from entangled atoms. *Phys. Rev. A*, 84:023805, Aug 2011.

[87] Lei Zhang, Leung-Kway Lee, Chu-Hsiang Teng, Tyler A. Hill, Pei-Cheng Ku, and Hui Deng. How much better are ingan/gan nanodisks than quantum wellsoscillator strength enhancement and changes in optical properties. *Applied Physics Letters*, 104(5):051116, 2014.

[88] Lei Zhang, Chu Hsiang Teng, Tyler A. Hill, Leung Kway Lee, Pei Cheng Ku, and Hui Deng. Single photon emission from site-controlled InGaN/GaN quantum dots. *Appl. Phys. Lett.*, 103(19):192114, 2013.

[89] Huaixiu Zheng and Harold U. Baranger. Persistent quantum beats and long-distance entanglement from waveguide-mediated interactions. *Phys. Rev. Lett.*, 110:113601, Mar 2013.